



Minidisk Accretion onto Spinning Black Hole Binaries: Quasi-periodicities and Outflows

Luciano Combi^{1,2}, Federico G. Lopez Armengol², Manuela Campanelli², Scott C. Noble³, Mark Avara⁴,

Julian H. Krolik⁵, and Dennis Bowen^{6,7}

¹ Instituto Argentino de Radioastronomía (IAR, CCT La Plata, CONICET/CIC), C.C.5, (1984) Villa Elisa, Buenos Aires, Argentina; lcombi@iar.unlp.edu.ar

² Center for Computational Relativity and Gravitation, Rochester Institute of Technology, Rochester, NY 14623, USA

³ Gravitational Astrophysics Laboratory, NASA Goddard Space Flight Center, Greenbelt, MD 20771, USA

⁴ Institute of Astronomy, University of Cambridge, Madingley Road, CB3 0HA, Cambridge, UK

⁵ Department of Physics and Astronomy, Johns Hopkins University, Baltimore, MD 21218, USA

⁶ Center for Theoretical Astrophysics, Los Alamos National Laboratory, P.O. Box 1663, Los Alamos, NM 87545, USA

⁷ X Computational Physics, Los Alamos National Laboratory, P.O. Box 1663, Los Alamos, NM 87545, USA

Received 2021 September 3; revised 2021 December 22; accepted 2022 February 7; published 2022 April 7

Abstract

We perform a full 3D general relativistic magnetohydrodynamical (GRMHD) simulation of an equal-mass, spinning, binary black hole approaching merger, surrounded by a circumbinary disk and with a minidisk around each black hole. For this purpose, we evolve the ideal GRMHD equations on top of an approximated spacetime for the binary that is valid in every position of space, including the black hole horizons, during the inspiral regime. We use relaxed initial data for the circumbinary disk from a previous long-term simulation, where the accretion is dominated by a $m = 1$ overdensity called the lump. We compare our new spinning simulation with a previous non-spinning run, studying how spin influences the minidisk properties. We analyze the accretion from the inner edge of the lump to the black hole, focusing on the angular momentum budget of the fluid around the minidisks. We find that minidisks in the spinning case have more mass over a cycle than the non-spinning case. However, in both cases we find that most of the mass received by the black holes is delivered by the direct plunging of material from the lump. We also analyze the morphology and variability of the electromagnetic fluxes, and we find they share the same periodicities of the accretion rate. In the spinning case, we find that the outflows are stronger than the non-spinning case. Our results will be useful to understand and produce realistic synthetic light curves and spectra, which can be used in future observations.

Unified Astronomy Thesaurus concepts: Supermassive black holes (1663); Jets (870); Compact objects (288); Magnetohydrodynamical simulations (1966)

1. Introduction

When two galaxies merge, a supermassive binary black hole (SMBBH) is expected to form (Merritt & Milosavljević 2005). The potential interaction of the new system with the surrounding gas and the dynamical friction of stars might shrink the binary separation to sub-parsec scales (Begelman et al. 1980; Escala et al. 2004, 2005; Merritt 2004, 2006; Dotti et al. 2007, 2009b; Mayer et al. 2007; Shi et al. 2012; Sesana & Khan 2015; Mirza et al. 2017; Khan et al. 2019; Tiede et al. 2020). At those separations, energy and angular momentum are extracted from the system by gravitational radiation until the BHs merge (Pretorius 2005; Baker et al. 2006; Campanelli et al. 2006a). In the near future, gravitational waves from SMBBH mergers might be observable in the mHz frequency band by the Laser Interferometer Space Antenna (LISA, Amaro-Seoane et al. 2017) and by *pulsar timing* techniques in the nHz range (Babak et al. 2016; Reardon et al. 2016; Alam et al. 2021).

Because the environment of these systems is most likely gas-rich, a SMBBH could also emit electromagnetic radiation through accretion (Barnes & Hernquist 1992, 1996; Mihos & Hernquist 1996; Mayer et al. 2007; Dotti et al. 2012; Mayer 2013; Derdzinski et al. 2019). At sub-parsec scales, SMBBHs cannot be spatially resolved and they might be hard

to distinguish from ordinary active galactic nuclei. There are many proposed signatures to identify the presence of a SMBBH using electromagnetic waves, for instance: Doppler variations due to the orbital motion (D’Orazio et al. 2015), binary periodicities in the light curves (Valtonen et al. 2006; Graham et al. 2015a, 2015b; Liu et al. 2019; Saade et al. 2020), interruption of jet emission (Schoenmakers et al. 2000; Liu et al. 2003) and “spin-flips” of the BH after merger (Merritt & Ekers 2002), dual-radio cores (Rodriguez et al. 2006), profile shifts of broad emission lines (Bogdanović et al. 2009; Dotti et al. 2009a), a “notch” in the optical/IR spectrum (Sesana et al. 2012; Roedig et al. 2014), periodicities in the thermal spectrum due to a short residence time for gas in the disk (Bowen et al. 2019), and X-ray periodicities (Sesana et al. 2012; Roedig et al. 2014). The feasibility of detecting some of these signatures depends strongly on binary properties such as mass-ratio and orbital separation (see also Krolik et al. 2019 for likely source counts).

Because the interstellar gas of the merged galaxy would have a considerable amount of angular momentum, a circumbinary disk should form around the binary (Springel et al. 2005; Chapon et al. 2013). For mass-ratios close to one, the system would present a gap of radius $\sim 2a$ between the binary’s semimajor axis a and the edge of the circumbinary disk. Accretion then occurs through two streams from the circumbinary to each black hole. Depending on its angular momentum, the material from the streams can eventually start orbiting the BHs, forming “minidisks.” On the other hand, the time-dependent quadrupole potential of the binary system can



Original content from this work may be used under the terms of the [Creative Commons Attribution 4.0 licence](https://creativecommons.org/licenses/by/4.0/). Any further distribution of this work must maintain attribution to the author(s) and the title of the work, journal citation and DOI.

induce a density concentration in the edge of the circumbinary disk on a small azimuthal range, breaking the axisymmetric accretion (MacFadyen & Milosavljević 2008). This feature is usually referred as the lump (Noble et al. 2012, 2021; Shi et al. 2012). When the lump is formed, it behaves as a coherent $m=1$ density mode orbiting the system at a frequency $\sim 0.25 \Omega_{\text{bin}}$, where Ω_{bin} is the binary frequency (Lopez Armengol et al. 2021; Noble et al. 2021). The time dependence of the gas available for the accretion onto the black holes is then dominated by the lump. If the residence time of the gas in the minidisks is shorter (or comparable to) the modulation period of the lump, then the accretion rate and luminosity of the minidisks are modulated by the lump (Bowen et al. 2018, 2019; d’Ascoli et al. 2018). Whether this modulation happens depends mostly on the orbital separation.

Numerical simulations are key tools to make accurate models from these highly nonlinear systems. Circumbinary BBH accretion has been largely investigated using viscous hydrodynamical models in 2D with Newtonian gravity (MacFadyen & Milosavljević 2008; D’Orazio et al. 2013, 2016; Farris et al. 2014a, 2014b; Muñoz & Lai 2016; Miranda et al. 2017; Derdzinski et al. 2019, 2021; Moody et al. 2019; Mösta et al. 2019; Muñoz et al. 2019, 2020; Duffell et al. 2020; Muñoz & Lithwick 2020; Tiede et al. 2020; Zrake et al. 2021). In these simulations, the system can be evolved for $\mathcal{O}(100\text{--}1000)$ binary orbits, when a relaxed stage is reached, and the effects of the initial conditions are suppressed. However, these simulations rely on artificial sink conditions for the black hole and their stress model is not self-consistent, i.e., they adopt an ad hoc description for the viscosity.

More realistic simulations using MHD have been performed in Newtonian gravity (Shi et al. 2012; Shi & Krolik 2015), in approximated General Relativity (GR; Noble et al. 2012, 2021; Zilhão et al. 2015; Bowen et al. 2018, 2019; Lopez Armengol et al. 2021), and in full numerical relativity (Farris et al. 2011; Giacomazzo et al. 2012; Cattorini et al. 2021; Paschalidis et al. 2021). MHD simulations are more computationally expensive than 2D α -viscous simulations because they demand 3D domains and fine resolutions. Moreover, general relativistic magnetohydrodynamical (GRMHD) simulations including both the minidisks and the circumbinary disk need to resolve different dynamical timescales and evolve the spacetime metric, and thus are usually too expensive to evolve for many orbits.

Because the properties of the minidisks are necessarily tied to the circumbinary accretion, it is important to perform simulations linking these regimes in order to obtain a proper global description of the system. A viable method to accomplish this was presented in Bowen et al. (2018), where a snapshot of an evolved circumbinary disk simulation (Noble et al. 2012) was used as initial data for studying minidisk accretion onto non-spinning black holes. In this way, Bowen et al. (2019) showed that minidisks at close binary separations exhibit a quasi-periodic filling and depletion cycle determined by the lump and the short inflow time of the minidisks.

An important property of supermassive black holes that many of these studies miss is the spin (Lin & Papaloizou 1979). When BBHs are approaching merger, spins can have an important impact on the spacetime evolution: they can alter the orbital motion of the system (Campanelli et al. 2006b; Hemberger et al. 2013; Healy & Lousto 2018), induce precession and nutation (Campanelli et al. 2007), repeatedly

flip their sign (Lousto & Healy 2015, 2019; Lousto et al. 2016), and even tilt the orbital orientation (Kesden et al. 2014). Spins also have a key role in the accretion of matter into BHs (Krolik et al. 2005) and BBHs. For instance, accretion rate per unit mass near the circumbinary disk’s inner edge depends on the spin, altering the mass profile in the inner part of the disk (Lopez Armengol et al. 2021). Moreover, the character of the flow within the minidisks depends on the ratio between the radius at which they are fed and the radius of the innermost stable circular orbit (ISCO; Bowen et al. 2018; Paschalidis et al. 2021), which is strongly dependent on the spin.

On the other hand, spinning black holes are expected to launch electromagnetic outflows (De Villiers & Hawley 2003; Hirose et al. 2004; McKinney & Gammie 2004; De Villiers et al. 2005; Krolik et al. 2005; Tchekhovskoy 2015). The generation of a net Poynting flux in a BBH system approaching merger has been modeled within general relativistic force-free electrodynamics (GRFFE; Palenzuela et al. 2010a, 2010b; Neilsen et al. 2011; Moesta et al. 2012) and ideal GRMHD (Farris et al. 2012; Giacomazzo et al. 2012; Kelly et al. 2017, 2021; Paschalidis et al. 2021). In the force-free regime, given a homogeneous plasma threaded by a constant magnetic field, the Blandford–Znajek (BZ) mechanism (Blandford & Znajek 1977) proved to operate efficiently around each BH, leading to a pair of collimated jets in a double-helical structure that coalesces after merger (Palenzuela et al. 2010a). The dynamics of BBHs in a homogeneous medium have also been investigated in the ideal GRMHD regime, where the inertia of the plasma is taken into account. In this case, accretion of the plasma onto the BHs leads to a steeper growth of the initial magnetic field during the inspiral, via compression and magnetic winding, resulting in higher luminosities (Giacomazzo et al. 2012). At the same time, the inertia of the (homogenous) plasma falling onto the BHs interferes with the propagation of the electromagnetic flux, causing fewer collimated magnetic structures compared with GRFFE (see also Kelly et al. 2017, 2021). Further, Farris et al. (2012), and Paschalidis et al. (2021) performed GRMHD simulations that include the circumbinary disk in the domain and also found the development of net Poynting fluxes emitted from the polar regions of each BH that coalesce at larger distances.

There are only a few GRMHD simulations of circumbinary accretion into spinning SMBBH. Very recently, Lopez Armengol et al. (2021) presented the first long-term circumbinary GRMHD simulation of spinning black holes (with the inner cavity excised), and Paschalidis et al. (2021) presented the first numerical relativity simulation of minidisks around spinning BHs, confirming previous expectations that the ISCO plays a key role in the minidisk mass (Bowen et al. 2018, 2019). A natural next step is to consider more realistic simulations where both minidisks and a properly relaxed circumbinary disk around spinning BBHs are taken into account. This is important to make accurate predictions of the light curves and spectra of these systems.

In this work, we present the results of a GRMHD simulation of minidisk accretion around spinning black holes of spins $a = 0.6M$ aligned with the orbital angular momentum. We evolve the ideal GRMHD equations on top of a BBH spacetime that is moving on a quasi-circular orbit starting at $20M$ separation. We use an approximate BBH spacetime that uses Post-Newtonian (PN) trajectories for the BHs in the inspiral regime, but is valid at every space point, including the BH

horizons. As initial data for the plasma, we use a steady-state snapshot of a circumbinary disk simulation performed in Noble et al. (2012). We compare our new simulation with a previous non-spinning simulation (Bowen et al. 2018, 2019) that uses the same initial data. In Section 2, we present the simulations setup, the numerical methods, the spacetime approximation that we use, and the initial data. In Section 3, we present our results. First, we give an overview of the main features of the system and the relation with previous simulations. In Section 3.2 we investigate the accretion rate, inflow time, and mass evolution of the minidisks, and in Section 3.3 we analyze the minidisks’ structure, the specific angular momentum distribution, and the azimuthal density modes. Then, in Section 3.4, we analyze the outflows, the magnetized structure of the system, and the variability of the Poynting flux, comparing spinning and non-spinning results. Finally, in Section 4 we discuss some of the implications of our results, and in Section 5, we summarize the main points and results of the paper.

Notation and conventions. We use the signature $(-, +, +, +)$ and we follow the Misner–Thorne–Wheeler convention for tensor signs. We use geometrized units, $G=c=1$. We use Latin letters $a, b, c, \dots = 0, 1, 2, 3$ for four dimensional components of tensors, and $i, j, k, \dots = 1, 2, 3$ for space components.

2. Simulation Setup

We evolve the equations of ideal GRMHD in the spacetime of a binary black hole system using the finite-volume code HARM3D. Our goal is to analyze the effects of the black hole spin in the minidisks. For that purpose, we compare two simulations of an equal-mass binary black hole, with and without spins. The non-spinning simulation, denoted as $S0$, was performed in Bowen et al. (2019) using an analytical metric built by matching different spacetimes (Mundim et al. 2014). We perform a new simulation, denoted $S06$, with BHs having spins of $\chi=0.6$ aligned with the orbital angular momentum of the binary, using an approximate analytical metric described in Combi et al. (2021); a concise summary is given in Section 2.3. For both simulations, we use the same grid and initial data in order to have a faithful comparison (see Section 2.3 for details).

2.1. GRMHD Equations of Motion

Assuming that the plasma does not influence the spacetime, we evolve the ideal GRMHD equations in the dynamical BBH metric described in Section 2.3. The equations of motion are given by the conservation of the baryon number, the conservation of the energy-momentum tensor, and Maxwell’s equations with the ideal MHD condition:

$$\begin{aligned} \nabla_a(\rho u^a) &= 0, & \nabla_a T^a_b &= \mathcal{F}_b, \\ \nabla_a {}^*F^{ab} &= 0, & u_a F^{ab} &= 0, \end{aligned} \quad (1)$$

where ρ is the rest-mass density, $F^{ab}/\sqrt{4\pi}$ is the Faraday tensor,⁸ u^a is the four-velocity of the fluid, \mathcal{F}_b is the radiated energy-momentum per 4-volume unit, and the MHD energy-

momentum tensor is

$$T^{ab} := (\rho h + b^2)u^a u^b + \left(P, +, \frac{1}{2}, b^2 \right) g^{ab} - b^a b^b \quad (2)$$

where $h := (1 + \epsilon + P/\rho)$ is the specific enthalpy, ϵ is the specific internal energy, P is the pressure, $b^a := {}^*F^{ab} u_b$ is the four-vector magnetic field, and $b^2 := b^a b_a$ is proportional to the magnetic pressure, $p_m := b^2/2$. We follow Noble et al. (2012, 2009) and write these coupled equations of motion in manifest conservative form as

$$\partial_t \mathbf{U}(\mathbf{P}) = -\partial_i \mathbf{F}^i(\mathbf{P}) + \mathbf{S}(\mathbf{P}), \quad (3)$$

where \mathbf{P} are the *primitive* variables, \mathbf{U} the *conserved* variables, \mathbf{F}^i the *fluxes*, and \mathbf{S} the *source* terms. These are given explicitly as:

$$\mathbf{P} := [\rho, u, \tilde{u}^j, B^j], \quad (4)$$

$$\mathbf{U}(\mathbf{P}) = \sqrt{-g} [\rho u^t, T^t_t + \rho u^t, T^t_j, B^j], \quad (5)$$

$$\mathbf{F}^i(\mathbf{P}) = \sqrt{-g} [\rho u^i, T^i_t + \rho u^i, T^i_j, (b^i u^j - b^j u^i)], \quad (6)$$

$$\mathbf{S}(\mathbf{P}) = \sqrt{-g} [0, T^\kappa_\lambda \Gamma^\lambda_{t\kappa} - \mathcal{F}_t, T^\kappa_\lambda \Gamma^\lambda_{j\kappa} - \mathcal{F}_j, 0], \quad (7)$$

where g is the determinant of the metric, $\Gamma^\lambda_{\alpha\beta}$ are the Christoffel symbols, $u := \rho\epsilon$ is the internal energy, $\tilde{u}^j := u^j - g^{tj}/g^tt$ is the velocity relative to the normal spacelike hypersurface, and $B^j := {}^*F^{it}$ is the magnetic field, which is both a conserved and a primitive variable.⁹ We close the system with a Γ -law equation of state, $P = (\Gamma - 1)\rho\epsilon$, where we set $\Gamma = 5/3$.

The source term in the energy-momentum conservation ensures that part of the dissipated energy caused by MHD turbulence is converted to radiation that escapes from the system. We assume radiation is removed from each cell independently of all the others, isotropically in the fluid frame. In this way, we set $\mathcal{F}_a = \mathcal{L}_c u_\beta$, where \mathcal{L} is the cooling function. We use the prescription used in Noble et al. (2012) for the rest-frame cooling rate per unit volume \mathcal{L}_c :

$$\mathcal{L}_c = \frac{\rho\epsilon}{t_{\text{cool}}} \left(\frac{\Delta S}{S_0} + \left| \frac{\Delta S}{S_0} \right| \right)^{1/2}, \quad (8)$$

where t_{cool} is the cooling timescale where the disk radiates away any local increase in entropy, $\Delta S := S - S_0$, where $S := p/\rho^\Gamma$ is the local entropy. Our target entropy, $S_0 = 0.01$, is the initial entropy of each accretion disk in the simulation. The timescale t_{cool} is determined by the local fluid orbital period, following the prescriptions in Bowen et al. (2017) and d’Ascoli et al. (2018).

2.2. Code Details, Grid, and Boundary Conditions

We solve Equation (3) using the high-resolution, shock-capturing methods implemented in HARM3D. Following Noble et al. (2012), we use a piecewise parabolic reconstruction of the primitive variables for the local Lax–Friedrichs flux at each cell interface and the Flux CT method to maintain the solenoidal constraint (Tóth 2000). Once the numerical fluxes are found, the equations are evolved in time using the method of lines

⁸ Following Noble et al. (2009), we absorb the factor $1/\sqrt{4\pi}$ in the definition of the tensor F^{ab} .

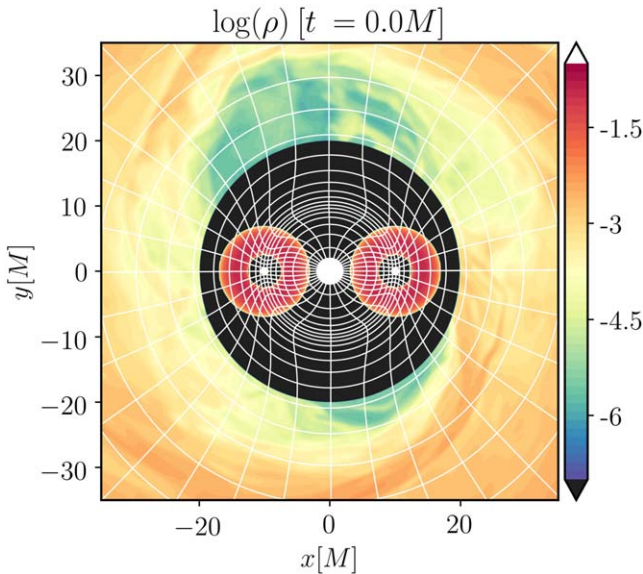


Figure 1. Initial data used in the simulation with quasi-equilibrated minitorus around the black holes. In white thin lines we plot the warped spherical grid every 50 cells.

with a second-order Runge–Kutta method. The primitive variables are recovered from the evolved conserved variables using the 2D method developed in Noble et al. (2006).

The grid and boundary conditions used in this simulation are the same as in Bowen et al. (2018, 2019). We use a time-dependent, double fish-eye, warped spherical grid, centered in the center of mass of the binary system, developed in Zilhão & Noble (2014; see full details of the grid used in Bowen et al. 2019). The maximum physical size of the grid is set to $r_{\max} = 13 r_{12}(0)$, containing the circumbinary disk of RunSE in Noble et al. (2012), that we use as initial data. We use outflow boundary conditions on the radial (x^1) boundaries, demanding the physical radial velocity u^r to be oriented out of the domain; if not, we reset the radial velocity to zero and solve for the remaining velocity components. Poloidal coordinates (x^2) have reflective, axisymmetric boundary conditions at the polar axis cutout and the azimuthal coordinates (x^3) have periodic boundary conditions.

The resolution is given by $600 \times 160 \times 640$ cells. The shape of the grid in the circumbinary region matches the grid used in Noble et al. (2012) and is sufficient to resolve the magnetorotational instability in the circumbinary disk. Because of our polar grid resolution and off-grid-center location of the BHs in the spherical grid, our configuration does not include a full 32 cells per scale height in the minidisks on the side farthest from the center of mass, see Figure 1.

2.3. BBH Spacetime and Initial Data

The spacetime of the binary black hole is approximated by superposing two Kerr spacetimes on a Minkowski background. We describe it in terms of harmonic coordinates. The metric can be written schematically as

$$g_{ab} = \eta_{ab} + M_1 \mathcal{H}_{ab}^1(\mathbf{x}_1, \mathbf{v}_1) + M_2 \mathcal{H}_{ab}^2(\mathbf{x}_2, \mathbf{v}_2), \quad (9)$$

where η_{ab} is the Cartesian Minkowski metric, \mathcal{H}_{ab}^A is the boosted black hole term for $A = 1, 2$, M_A is the mass, and $\{\mathbf{x}_A(t), \mathbf{v}_A(t)\}$ are the position and velocity of the black hole. The trajectories are obtained by solving the Post-Newtonian

equations of motion for a spinning BBH in quasi-circular motion at 3.5 PN order. In Combi et al. (2021), we showed that this analytical metric constitutes a good approximation to a vacuum solution of Einstein’s field equations for a BBH approaching merger; see also East et al. (2012), Varma et al. (2018), and Ma et al. (2021) for similar approaches in the context of numerical relativity. The metric (9) is computationally efficient, compared with previous approaches, and easy to handle for different parameters. In the non-spinning simulation, the spacetime was represented by an semi-analytical metric built by stitching different approximate solutions of Einstein’s equation (Mundim et al. 2014). In Combi et al. (2021), we compared the matching and superposed metrics evolving two GRMHD simulations for the non-spinning case, and we found that they are completely equivalent in this context. Moreover, we analyzed the spacetime scalars and integrated Hamiltonian constraints for each one, and we found that (a) they remain small and well behaved up to a separation of $10M$, and that (b) the constraints remain invariant when we change the BH spin, and thus no pathologies are introduced by the spin.

The level at which these constraints are violated is comparable to the very low level achieved in the numerical simulations performed in Zlochower et al. (2016), who used the matching metric as initial data for evolving Einstein’s equations. Constraint violations in this evolution, which can be damped using the CCZ4 scheme, mainly introduce deviations to the trajectories (eccentricity) and errors in the masses and spins of the BHs. In our analytical metric, however, there are no such dynamical effects because we solve the trajectories using the PN approximation and the BH masses/spins are fixed. The small constraint violations, relative to the mass of the BHs, might produce small errors in the gas dynamics, but these are washed out by MHD turbulence in our simulation (Zilhão et al. 2015).

Although the metric uses PN trajectories and thus is valid only in the inspiral regime, it is mathematically well defined at every point in space, including the horizons of the black holes; hence, no artificial sink terms or large excisions are needed in the evolution. We apply, however, a mask inside the horizon to avoid the singularity of each black hole. In particular, we do not evolve the hydro fluxes inside the masked region and we set to zero the magnetic fluxes. This allows us to evolve the induction equations in the whole domain and preserve the solenoidal constraints.

For this simulation, we use an equal-mass black hole binary, $M_1 = M_2 = M/2$, with an initial separation of $r_{12}(0) = 20M$, where relativistic effects are important (Bowen et al. 2017) and the orbit is shrinking due to gravitational radiation. In S06 we set the spins of the black holes perpendicular to the orbital plane (i.e., no precession) with a moderate value of $\chi \equiv a/M = 0.6$. Because spin couples with the orbital motion, the trajectories of the holes change with respect to a non-spinning system. In particular, the inspiral is delayed because of the *hang-up* effect (Campanelli et al. 2006c), and the orbital frequency increases (see Figure 2).

To compare with the previous simulation, we take the same initial data for the matter fields as in Bowen et al. (2018). We start with a snapshot of the circumbinary disk from Noble et al. (2012), previously evolved for $5 \times 10^4 M$ (~ 80 orbits). At this time, the disk is in a turbulent state and the accretion into the cavity is dominated by the $m = 1$ density mode, the so-called

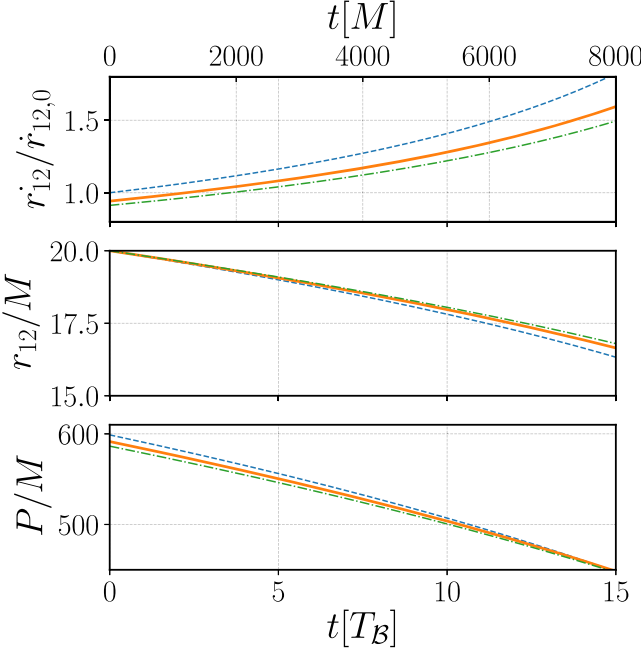


Figure 2. Properties of a binary black hole system with aligned spins of $\chi = 0.0$ (blue dashed line), $\chi = 0.6$ (solid orange line), and $\chi = 0.9$ (green dashed line). In the top panel, we plot the radial velocity, \dot{r}_{12} , normalized with its initial value; in the middle panel, the orbital separation r_{12} ; and in the bottom panel, the period of the orbit, P .

lump, that is orbiting at the inner edge of the circumbinary disk. In Noble et al. (2012) a zero spin PN metric in harmonic coordinates was used to evolve the system. As shown in Lopez Armengol et al. (2021), the bulk properties of the circumbinary disk are not sensitive to the spin, even for high values of spin, so it is a good initial state for our spinning simulation. We interpolate these data onto our grid and we initialize two minitori inside the cavity; see Figure 1. We then clean magnetic divergences introduced by the interpolation to the new grid using a projection method as explained in Bowen et al. (2018). Further details of the simulations setup are outlined in Table 1.

2.4. Diagnostics

Properties of the circumbinary disk and other global properties of the system are better analyzed in the center of mass coordinates. On the other hand, to analyze minidisks properties such as fluxes, we shall compute quantities on the (moving) BH frame. We define the BH frame at a given time slice with a boosted coordinate system centered at each BH (see Combi et al. 2021); we denote these BH coordinates with a bar, $\{\bar{t}, \bar{r}, \bar{\theta}, \bar{\phi}\}$. We notice that all our diagnostic are written in the harmonic coordinate gauge. Fluxes and other local properties in this frame are computed in post-process, interpolating the global grid into a spherical grid centered in the BH with the Python package `naturalneighbor`¹⁰, which implements a fast Discrete Sibson interpolation (Park et al. 2006).

Weighted surface averages of a MHD quantity \mathcal{Q} with respect to a quantity σ are defined as

$$\langle \mathcal{Q} \rangle_\sigma := \frac{\int dA \sigma \mathcal{Q}}{\int dA \sigma}, \quad (10)$$

Table 1
Physical and Grid Parameters of both Non-spinning and Spinning Simulations

Simulation	S06	S0
Spin parameter [χ]	0.6	0.0
BH _{1,2} mass [M_{BH}]	0.5	
Mass-ratio [q]	1	
Final time [t_f]	$8000M$	$6000M$
Final separation [$r_{12}(t_f)$]	$16.6M$	$17.8M$
# Orbit	15	12.5
Init. separation [$r_{12}(0)$]	$20M$	
Init. total minidisk mass [M_0]	20	
Average orbital period [T_B]	$530M$	
Lump orbital frequency [Ω_{lump}]	$0.28 \Omega_B$	
ISCO radius [r_{ISCO}]	$2.82 M_{\text{BH}}$	$5.0 M_{\text{BH}}$
Truncation radius [r_{trunc}]	$0.4 r_{12}$	
Grid [$(x^1 \times x^2 \times x^3)$]		$(600, 160, 640)$
Physical Size [(r_{\min}, r_{\max})]		$(2M, 260M)$

where $dA := d\theta d\phi \sqrt{-g}$. A time average of a surface-average is defined as

$$\langle\langle \mathcal{Q} \rangle\rangle := \frac{1}{\Delta t} \int_{t_f}^{t_i} dt \langle \mathcal{Q} \rangle, \quad (11)$$

where we always sum over a given time interval after the initial transient.

3. Results

3.1. Overview of the System and Previous Studies

In the steady state of an equal-mass SMBBH, a lump orbits the edge of the circumbinary disk at an average frequency $\langle \Omega_{\text{lump}} \rangle = 0.28 \Omega_B$ (Noble et al. 2012, 2021; Shi et al. 2012; D’Orazio et al. 2013, 2016; Farris et al. 2015a, 2015b; Lopez Armengol et al. 2021) modulating the accretion into the cavity. In Figure 3, we show a global look of the system. When one of the BHs passes near the lump, it peels off part of the lump’s inner edge, forming a stream that feeds the black hole with a beat frequency of $\Omega_{\text{beat}} := \Omega_B - \langle \Omega_{\text{lump}} \rangle \sim 0.72 \Omega_B$. This stream is almost ballistic, formed by fluid particles with relatively low angular momentum (Shi & Krolik 2015). As it approaches the black hole, this material can start orbiting the black hole, forming a minidisk. The maximum size of the minidisks is determined by the tidal truncation radius of the binary, or Hill’s sphere. The residence time of matter in the minidisks is determined by the ratio of the truncation radius and the radius of the ISCO. At close relativistic separations, such as the ones here, the minidisks will be out of inflow equilibrium with the circumbinary lump accretion, and thus the masses oscillate quasi-periodically in a filling and depletion cycle (Bowen et al. 2018, 2019).

For relativistic binaries, the tidal truncation radius is approximately at $r_t \sim 0.4 r_{12}(t)$ (Bowen et al. 2017), similar to the Newtonian value, estimated to be $\sim 0.3 r_{12}$ (Paczynski 1977; Papaloizou & Pringle 1977; Artymowicz & Lubow 1994). Because spin is a second-order effect in the effective potential (Lopez Armengol et al. 2021), mild values of spin do not change the truncation radius significantly for binary separations greater than $20M$. The most relevant difference between our two simulations S06 and S0 is the location of the ISCO: $r_{\text{ISCO}}(\chi = 0.6) = 2.82 M_{\text{BH}}$ for S06, and $r_{\text{ISCO}}(\chi = 0.0) = 5.0 M_{\text{BH}}$ for S0 (both in given here in

¹⁰ <https://github.com/innolitics/natural-neighbor-interpolation>

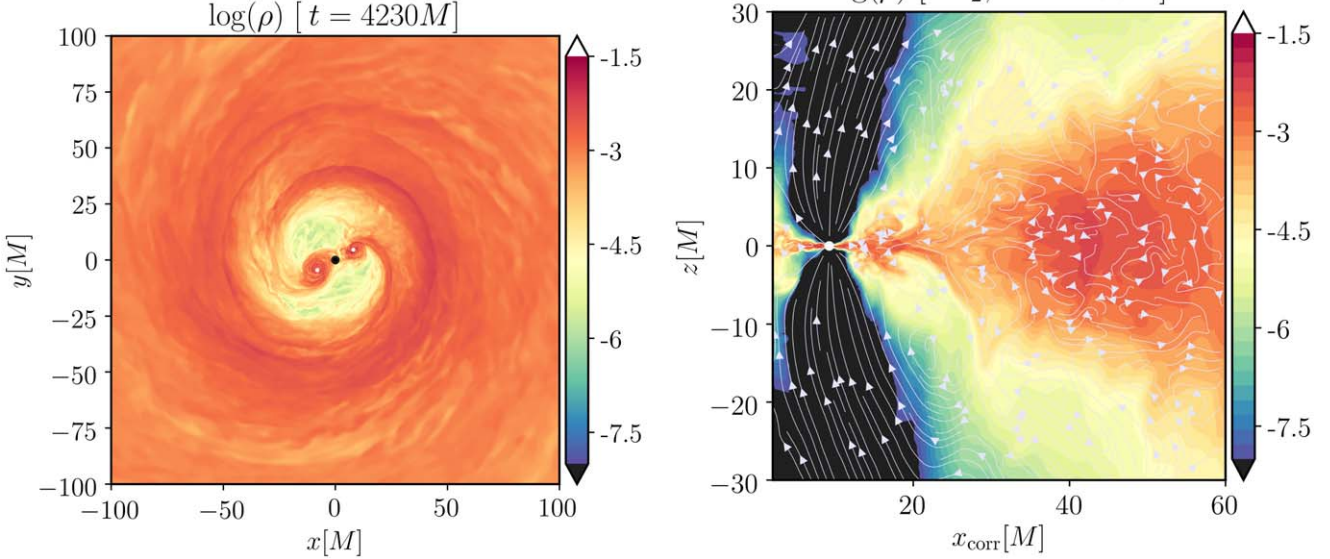


Figure 3. Left panel: Rest-mass density snapshot of the fluid in the equatorial plane for S06. Right panel: Rest-mass density snapshot of the fluid in the meridional plane corrotating with the (second) black hole. White stream lines represent the comoving magnetic field projected on the meridional plane.

harmonic coordinates). The smaller ISCOs of the spinning black holes allow material with lower angular momentum to maintain circular orbits closer to the BH instead of plunging in directly (see Section 3.3).

In the following sections, we analyze how the size of the ISCO plays a role in the accretion rate, inflow time, and periodicities, as well as in the structure of the minidisks. We will also examine how the presence of an ergosphere in the spinning case helps the black holes to produce more Poynting flux. We will also analyze how the variability of the fluxes is connected with the variability of the accretion rate, dominated by the lump.

3.2. Mass Evolution, Accretion Rate, and Inflow Time

We start the analysis by calculating the integrated rest-mass of each minidisk, defined as

$$M := \int_{r_{\mathcal{H}}}^{r_i(t)} dV \rho u^t, \quad (12)$$

where $r_i(t) := 0.4 r_{12}(t)$ is the truncation radius, $r_{\mathcal{H}}$ is the BH horizon, and $dV := \sqrt{-g} d^3x$ is the volume element. In both simulations there is an initial transient due to the initial conditions that lasts approximately ~ 3 orbits for S0 and ~ 4 orbits for S06 (see Figure 4). Both simulations start with two quasi-equilibrated minitori around the holes, with a specific angular momentum distribution adapted specifically for non-spinning black holes, following the prescription described in Bowen et al. (2017). Because we are also using these initial data for the spinning simulation, the initial tori have an excess of angular momentum, making the transient slightly longer in S06. We analyze each simulation after this transient, marked in the plots as a vertical line. As a time unit, we use $T_B = 530 M$, the average binary period of the spinning simulation.

We find that although the minidisks of S06, like those in S0, go through a filling-depletion cycle, the minidisks around spinning BHs in S06 are more massive than in S0 by a factor of 2 through most of the evolution (Figure 4), although they

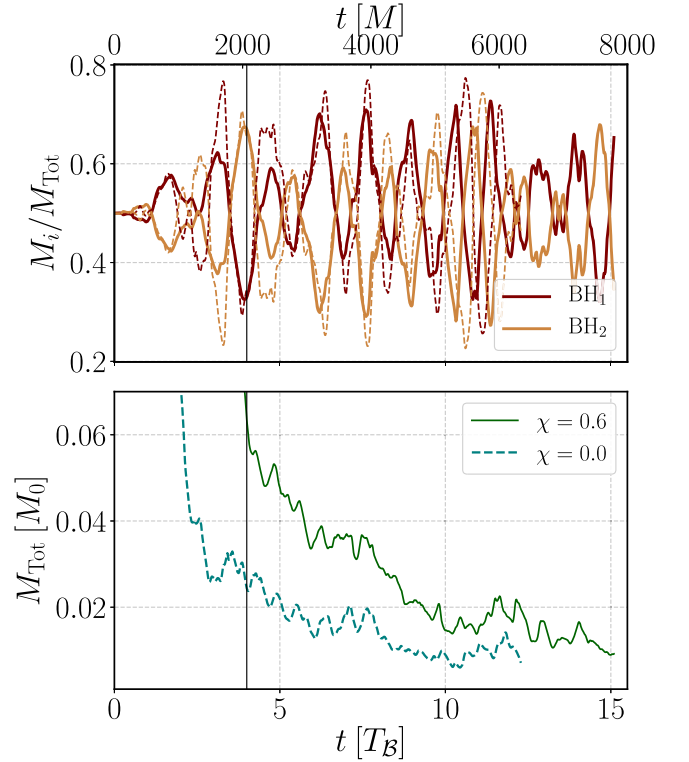


Figure 4. Upper panel: the mass fraction evolution M_i of each minidisk for S06 (solid lines) and S0 (dashed lines), where we define $M_{\text{tot}} := M_1(t) + M_2(t)$. Lower panel: total mass evolution for S06 (solid line) and S0 (dashed line), where $M_0 := M_1(0) + M_2(0)$. The black line indicates the end of the transient phase.

both follow the same decay. When the mass fraction of a minidisk is more than 50% of the total mass, we say that the disk is in its *high state*; otherwise, it is in its *low state*. The cycle of the mass fraction is similar in both simulations, although marginally smaller in amplitude for S06. The frequency of the cycle is associated with the orbital frequency and thus is higher in the spinning case, as can be seen plainly

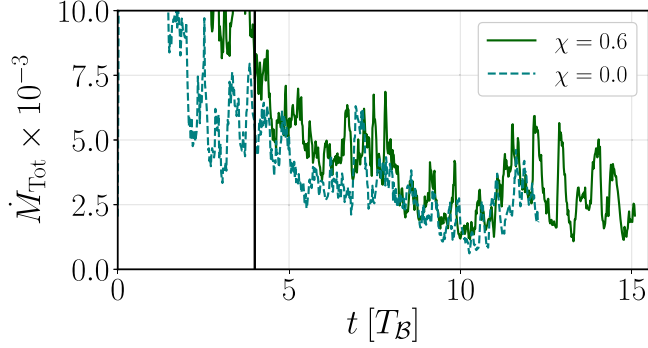


Figure 5. Total accretion rate evolution $\dot{M}_{\text{Tot}} \equiv \dot{M}_{\text{BH}_2} + \dot{M}_{\text{BH}_1}$ in S06 (solid lines) and S0 (dashed lines).

after ~ 8 orbits (upper panel, color blue, of Figure 4). On the other hand, at $t = 11 T_B$, we observe a slight increase of mass in the system. Because the lump grows and oscillates radially around the cavity (Lopez Armengol et al. 2021), it generates stronger accretion events onto the black holes with a lower frequency (see below).

We also analyze the accretion rate evolution at the horizon in the black hole rest frame, which is given by

$$\dot{M} := \oint_{r_h} d\bar{A} u^{\bar{r}} \rho. \quad (13)$$

Here and in the remainder of this paper, overbars indicate (harmonic) coordinates whose origin is the center of one of the black holes. We plot the sum of the accretion rate in each BH, \dot{M}_{Tot} , for each simulation in Figure 5. We find that the accretion rate evolution is overall similar after the transient in both S06 and S0. Moreover, the time dependence of the minidisk mass is, to a first approximation, a smoothed version of the accretion rate's time dependence, e.g., see Figure 6 for \dot{M}_{BH_1} in S06.

The differences in the masses per cycle are closely related to the inflow time of particles in the minidisk. It is useful then to define an (Eulerian) inflow time as the characteristic time for a fluid element to move past a fixed radius r (Krolik et al. 2005). On average, this can be defined as

$$t_{\text{inflow}}^{-1} := \frac{1}{\bar{r}} \langle \langle V^{\bar{r}} \rangle_{\rho} \rangle, \quad (14)$$

where $V^{\bar{r}} := u^{\bar{r}}/u^{\bar{t}}$ is the transport velocity. In Figure 7, we show the inflow time as a function of coordinate radius for BH_1 , averaged in time for the first part (solid lines) and second part (dashed lines) of both simulations. Inside the truncation radius, the inflow time is consistently longer in S06 than in S0, generally by tens of percent.

As the binary shrinks, the inflow time at the truncation radius diminishes from $\sim 0.41 T_B$ to $\sim 0.31 T_B$ for the spinning simulation. The average inflow time at the truncation radius is well below the beat period, $T_{\text{beat}} = 1.3 T_B$, on which the minidisk refills. Our mean inflow time is also significantly shorter than typical inflow timescales of Keplerian orbits around single black holes (Krolik et al. 2005). This suggests that accretion in our minidisks is driven by different mechanisms than single BH disks. Moreover, the similar measures of accretion rates at the horizon for S06 and S0 (see again Figure 5) seem to imply a shared accretion mechanism between spinning and non-spinning systems (see Section 3.3).

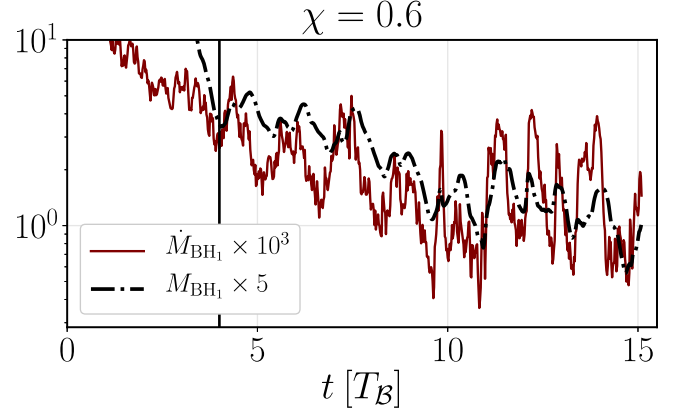


Figure 6. Accretion rate (\dot{M}_{BH_1}) in red solid lines and mass (M_{BH_1}) in black dotted-dashed lines for a minidisk around BH_1 in S06. Both quantities were rescaled for plotting.

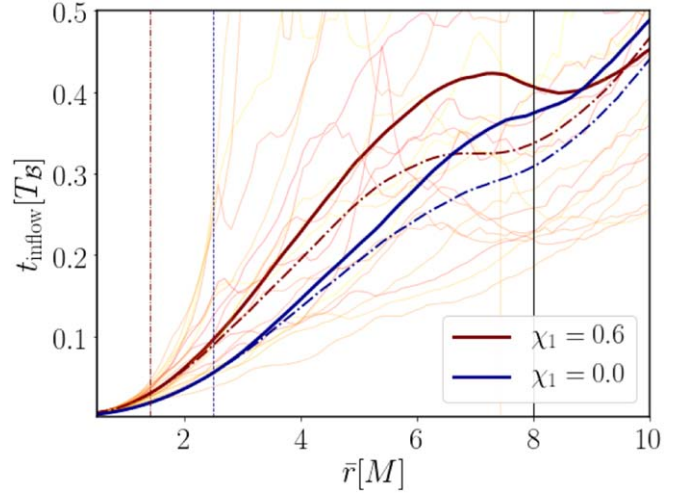


Figure 7. Inflow time as a function of radius in harmonic coordinates for BH_1 in S06 (maroon) and S0 (dark blue). Solid lines are time averages over the first half of the simulation, while dotted-dashed lines are time averages of the last half of the simulation. Thin lines show the instantaneous inflow time every $300M$ for the spinning case. The maroon (dark blue) vertical line represents the ISCO of the spinning (non-spinning) black hole. The vertical black line is the initial truncation radius of the binary.

The quasi-periodic behavior of the system can be described through a power density spectrum (PSD) of the minidisk's masses. In Figure 8 we show the PSD, normalized with the power of the highest peak within the simulation. Most features of the system's quasi-periodicities are shared in both simulations and were described in detail in Bowen et al. (2019). We find, still, some interesting differences. The PSDs for M_1 and M_2 taken individually peak at the beat frequency in both simulations. The PSD of the total mass of the minidisks, $M_1 + M_2$, has a peak at $2\Omega_{\text{beat}}$ in S0, while the latter is severely damped in S06. Indeed, if the individual masses vary with a characteristic frequency Ω_{beat} , and these are out of phase with the same amplitude, we expect their sum to vary with $2\Omega_{\text{beat}}$. In S06, however, the inflow time of the minidisks is larger and the depletion period of a minidisk briefly coexists with the filling period of the other minidisk, reducing the variability of the total mass. On the other hand, the beat frequency is slightly higher for S06 ($\Omega_{\text{beat}} = 0.71\Omega_B$) than S0 ($\Omega_{\text{beat}} = 0.68\Omega_B$) as the orbital frequency of the spinning BHs is higher. Further, because we evolved the binary for longer, in S06 we find a

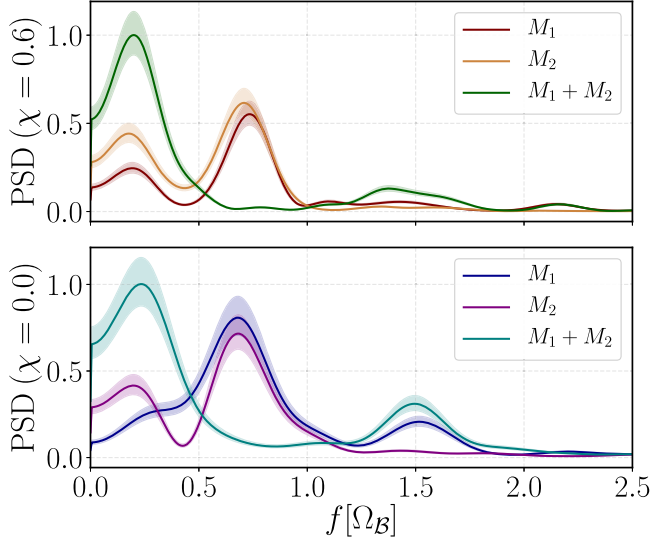


Figure 8. Power spectral density of the minidisk's masses for S06 (upper panel) and S0 (lower panel) using a Welch algorithm with a Hamming window size and a frequency of $10M$. The confidence intervals at 3σ are shown as shadowed areas.

more prominent amplitude at $\sim 0.20\Omega_B$. We can associate this low-frequency power to the radial oscillations of the lump around the cavity that produces additional accretion events (Lopez Armengol et al. 2021). We observe that this frequency is closely related but different from the orbital frequency of the lump at $0.28\Omega_B$, which could be related to the orbital frequency increasing during the inspiral (notice we measure the PSD at fixed frequencies).

Finally, because we use a spherical grid with a central cutout, we cannot analyze the effects of the sloshing of matter between minidisks (Bowen et al. 2017). To estimate how much mass we lose through the cutout, we compute the accretion rate at the inner boundary of the grid. This mass loss constitutes only 5% of the total mass accreted by the BHs throughout the simulation, although the instantaneous accretion can be close to 20% of the accretion onto a single BH. We do not expect this small mass loss to alter the main conclusions of this work, namely, the differences between minidisks in spinning and non-spinning BBH.

3.3. Structure and Orbital Motion in Minidisks

In this section, we analyze in detail how the structure of the minidisks in S06 compares with minidisks in S0. We first focus on how the spin changes the surface density distribution and the azimuthal density modes in the minidisks. We then investigate the angular momentum of the fluid and how it compares with the angular momentum at the ISCO.

The surface density is defined as $\Sigma(t, r, \phi) := \int d\theta \rho \sqrt{-g} / \sqrt{-\sigma}$, where we use $\sqrt{-\sigma} = \sqrt{g_{\phi\phi} g_{rr}}$ as the surface metric of the equatorial plane. In Figure 9, we plot the surface density in both S06 and S0, for the same orbital phase at the seventh orbit. In this plot, the minidisk around BH₁ (right side) is in the peak of the mass cycle. In both simulations we can clearly notice the lump stream plunging directly into the hole. There is also circularized gas orbiting BH₁ in both simulations, but there is much more of it in S06. On the other hand, we observe that BH₂ (left side), in its low state, has a noticeable disk structure in S06, while the material is already depleted for S0.

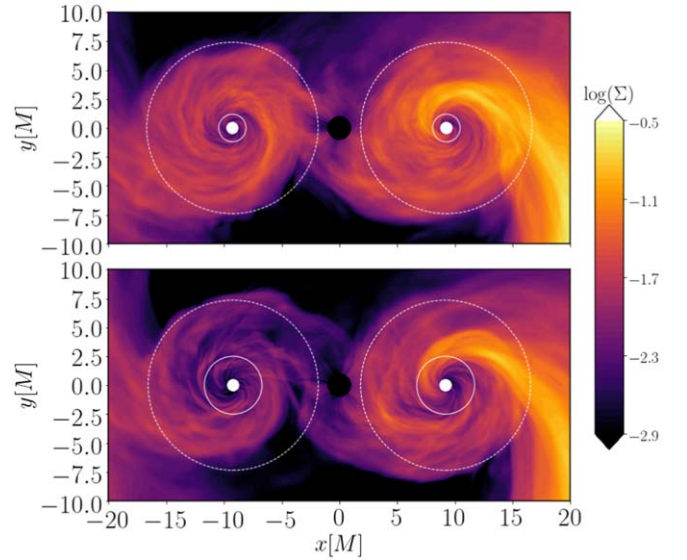


Figure 9. Surface density snapshot for S06 (upper row) and S0 (lower row) at $t = 4000M$ and $t = 4060M$ respectively, where the phase of the binary is the same in both simulations. White dashed lines indicate the truncation radius and solid white lines indicate the ISCO. The sense of rotation of the binary is counter-clockwise.

We can quantify these differences in structure by computing the average surface density over two ranges of $\bar{\phi}$, as measured in the BH frame, representing the front and back of the minidisk with respect to the orbital motion. We define

$$\langle \Sigma(r, t) \rangle := \frac{\int_{\Delta\bar{\phi}} d\bar{\phi} \Sigma}{\int_{\Delta\bar{\phi}} d\bar{\phi}}, \quad (15)$$

where $d\bar{\phi} := d\bar{\phi} \sqrt{g_{\bar{\phi}\bar{\phi}}} (\bar{\theta} = \pi/2)$. In Figure 10, we plot $\langle \langle \Sigma(r) \rangle \rangle$ for $\Delta\bar{\phi}_1 = (\pi/4, 3\pi/4)$ and $\Delta\bar{\phi}_2 = (5\pi/4, 7\pi/4)$, averaging in time over the high and low state of the minidisk separately. In the high state, the minidisk accumulates more material at the front, while the back of the minidisk is flatter. In the low state, both simulations show a flatter profile, with a slightly higher density at the front. The asymmetry between front and back arises because of the orbital motion of the black holes, capturing and accumulating the stream material as they orbit. In S06, the density profile is steeper near the ISCO for high and low states. In the outer part of the minidisk, the slope of the surface density for both S0 and S06 have a similar profile, indicating a common truncation radius. The density is higher in S06 by a factor of ~ 2 in both states.

Another important property of minidisks in relativistic binaries is the presence of nontrivial azimuthal density modes. When the accreting stream of the lump impacts the minidisk, it generates a pressure wave, forming strong spiral shocks (Bowen et al. 2018). This induces an $m = 1$ density mode in the minidisk that competes with the $m = 2$ mode excited by the tidal interaction of the companion black hole. The spiral wave patterns can be analyzed decomposing the minidisk rest-mass density in azimuthal Fourier modes (Zurek & Benz 1986), $\rho(\bar{\phi}) \equiv \sum_m D_m \exp(-im\bar{\phi})$, where

$$D_m := \int_{r_H}^{r_f(t)} d\bar{V} \rho \exp(-im\bar{\phi}). \quad (16)$$

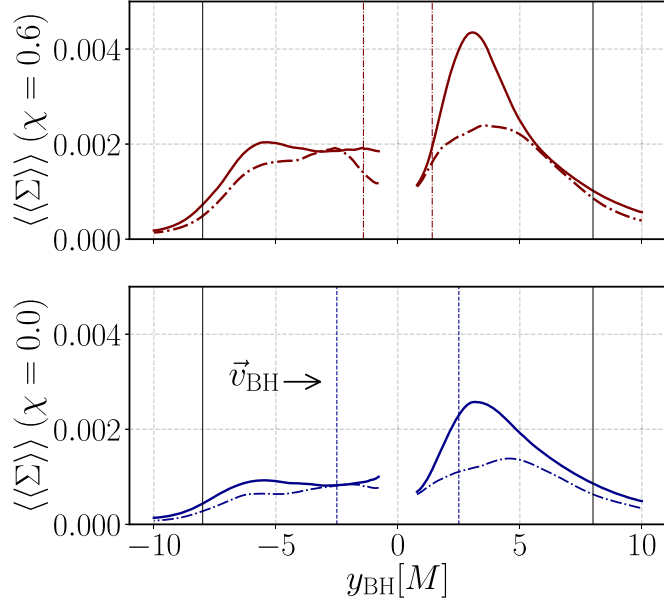


Figure 10. Surface density average in the azimuthal ranges $\Delta\phi_1 = (\pi/4, 3\pi/4)$ (positive y_{BH} -axis) and $\Delta\phi_2 = (5\pi/4, 7\pi/4)$ (negative y_{BH} -axis) for BH_1 in S06 (upper panel) and S0 (lower panel). Solid lines represent a time average on the high state of the cycle, while dotted-dashed lines represent a time average over the low state. For reference, we indicate the direction of the orbital BH velocity.

Let us compare these modes in S0 and S06 for BH_1 . From Figure 11, we observe that both simulations share common features. In both simulations, the minidisks are mainly dominated by $m = 1$ modes, followed closely by $m = 2$ modes. We also observe important $m = 3, 4$ contributions. The modes are excited in the high state of the cycle, where the minidisks increase their mass and the stream is accreted into the black holes. In S0, the amplitudes of the modes are noticeably larger than S06, while in the latter the amplitudes grow as the system evolves. The growth of modes in S06 is correlated with the mass decrease of the minidisks. This behavior could indicate that, as the minidisks become less massive, the density modes are really representing the single-arm stream of the lump that plunges directly into the hole. Azimuthal modes grow to large amplitudes in the high phase of a minidisk only when the material orbiting the BH is less or equally massive than the material with low angular momentum that plunges from the lump, occurring around $10T_B$ in S06 (see Figure 13 and discussion below). This is another consequence of the disk-like structure of the minidisks surviving for longer time in the spinning case.

Our analysis so far indicates that a considerable amount of the matter in the minidisk region is plunging directly from the lump to the black hole. To further analyze the orbital motion of the fluid in the minidisk, we compute the density-weighted specific angular momentum in the BH frame $\langle \bar{\ell} \rangle_\rho$, where $\bar{\ell} := -u_{\bar{\phi}}/u_{\bar{r}}$. In Figure 12, we show the time average of $\langle \bar{\ell} \rangle_\rho$ for both BHs and both simulations. In absolute terms, $\langle \bar{\ell} \rangle_\rho$ is nearly the same for both the spinning and non-spinning cases, with the spinning case only slightly greater. This is because the specific angular momentum of the material that falls into the cavity is essentially determined by the stresses at the inner edge of the circumbinary disk. These stresses are determined by

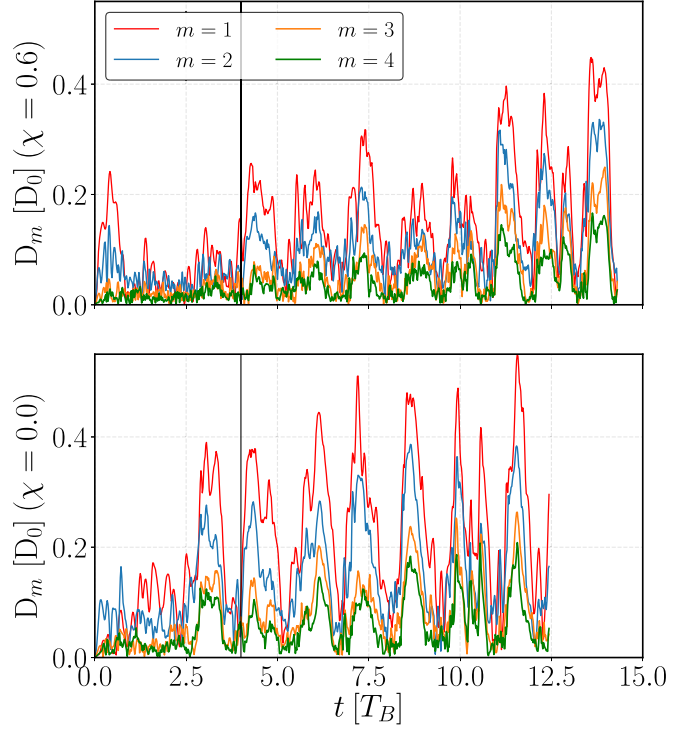


Figure 11. Azimuthal density modes for BH_1 in S06 (upper panel) and S0 (lower panel) normalized with the zero mode D_0 . The black vertical line represents the end of the transient in S06.

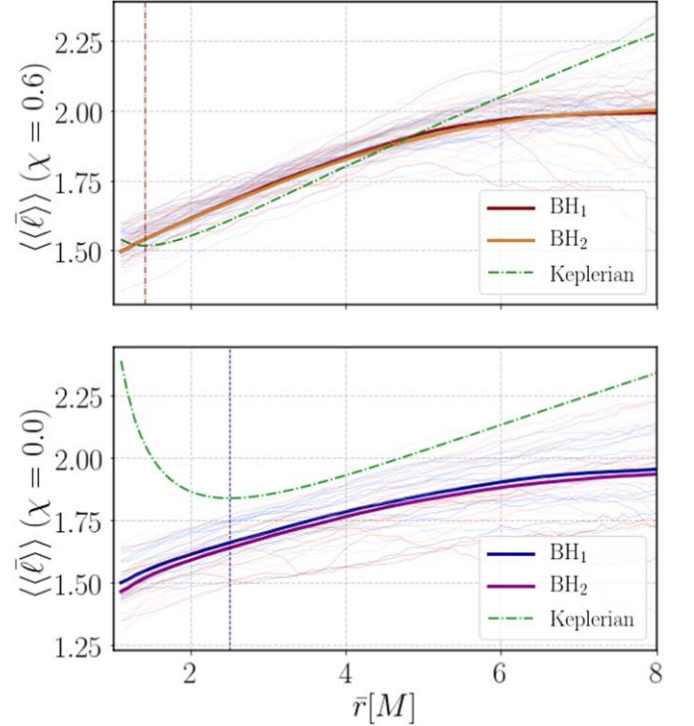


Figure 12. Specific angular momentum as a function of radius for S06 (upper panel) and S0 (lower panel) for both BHs. The time averages are in solid lines, and the individual values are the very thin lines. The Keplerian value is plotted in dashed green lines.

binary torques and the plasma Reynolds and magnetic stresses (Noble et al. 2012; Shi et al. 2012). Indeed, in Lopez Armengol et al. (2021) we found that these quantities depend weakly on

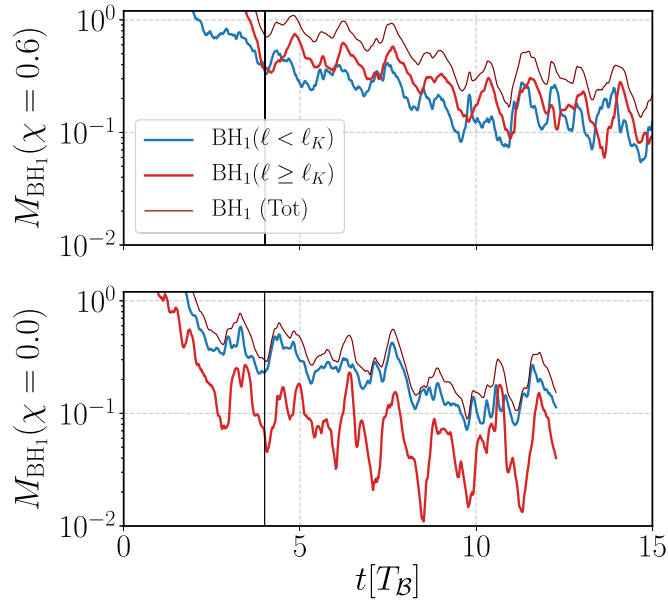


Figure 13. Sub-Keplerian and (super-)Keplerian components of the mass for BH_1 in $\text{S}06$ (upper panel) and $\text{S}0$ (lower panel).

spin outside the cavity. On the other hand, their relation to their respective circular orbit values, $\bar{\ell}_K(\bar{r}, \chi)$, is quite different because they depend strongly on the spin. In $\text{S}06$, the distribution of the angular momentum tracks closely to the Keplerian value. For $\text{S}0$, the behavior is always sub-Keplerian on average. If the angular momentum distribution of the circumbinary streams is independent of spin for a fixed binary separation and mass-ratio, the angular momentum with which the streams arrive at the minidisks is greater than the ISCO angular momentum for spin $\chi > 0.45$. This estimate could serve as a crude criterion for determining whether minidisks form in relativistic binaries.

We can also use the specific angular momentum to distinguish the material in the minidisks with high angular momentum that manages to orbit the black hole from the low angular momentum part that plunges in. To do so, we recompute the mass as in Equation (12), taking fluid elements with $\bar{\ell} < \bar{\ell}_K$ and $\bar{\ell} \geq \bar{\ell}_K$ separately. In Figure 13 we plot the evolution of the sub-Keplerian and super-Keplerian mass components for BH_1 in $\text{S}06$ and $\text{S}0$. In $\text{S}06$ after the initial transient, a little more than half of the mass comes from relatively high angular momentum fluid. As the system inspirals, however, the truncation radius decreases, and the masses of these two components become nearly equal. In $\text{S}0$, on the other hand, most of the fluid has relatively low angular momentum. This sub-Keplerian component has roughly the same mass in $\text{S}06$ and $\text{S}0$, while the mass of the high angular momentum component of the fluid is much greater in $\text{S}06$, as expected.

Although a fair amount of the mass in the minidisks has relatively high angular momentum and manages to orbit the black hole in $\text{S}06$, the accreted mass onto the BH, in both simulations, is always dominated by the low angular momentum part that plunges directly. To demonstrate this, we compute the average accretion rates for low and high angular momentum particles as we did with the mass. Figure 14 shows that the total accretion rate onto the BH has a flat radial profile in both $\text{S}06$ and $\text{S}0$, with very similar average values. Accretion by low angular momentum particles dominates at all

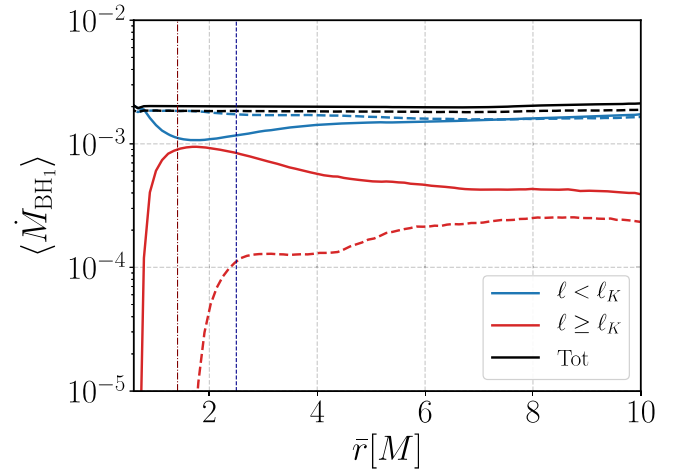


Figure 14. Time averaged accretion rate in BH_1 for $\text{S}06$ (solid lines) and $\text{S}0$ (dashed lines) considering particles with low (blue) and high (red) angular momentum. The vertical dashed blue and dotted-dashed red lines mark the ISCO for $\text{S}0$ and $\text{S}06$, respectively.

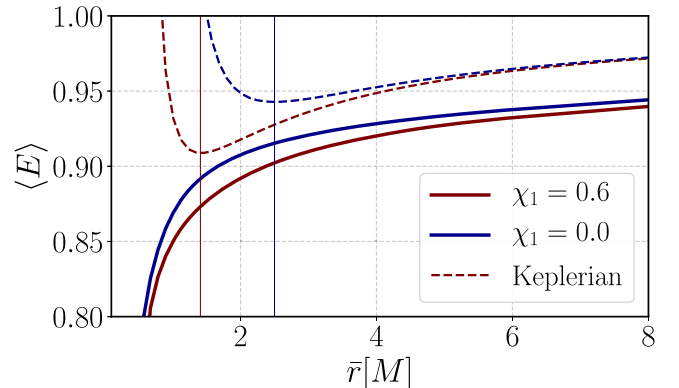


Figure 15. Density-weighted specific energy $E = -u_i$, averaged in time as a function of radius for BH_1 in $\text{S}06$ and $\text{S}0$. The dashed line represents the specific energy for a geodesic particle in circular motion in each case. Vertical lines indicate the location of the ISCO.

radii, although the high angular momentum contribution becomes comparable to the low angular momentum one near the ISCO for $\text{S}06$.

We can also compute the density-weighted specific energy, $E := \langle -u_i \rangle_\rho$, the mass-weighted sum of rest-mass, kinetic, and binding energy for individual fluid elements. As can be seen in Figure 15, on average, fluid in the minidisks around the spinning black holes is more bound than in the non-spinning case. On the other hand, fluid in both $\text{S}06$ and $\text{S}0$ is more bound than particles on circular orbits. Near the ISCO, the specific energy drops sharply inward in both cases, as is often found when accretion physics is treated in MHD: stress does not cease at the ISCO when magnetic fields are present.

When the minidisk is in its high state, the spiral shocks heat up the minidisks and increase their aspect ratio, h/r . Given our cooling prescription, the entropy is kept close to its original value, regulating the aspect ratio to $h/r = 0.1$. However, the gas scale height increases dramatically where the lump stream impacts the minidisk. At the peak of the accretion cycle, the aspect ratio rises to $h/r \sim 2$, but the gas cools before the next accretion event.

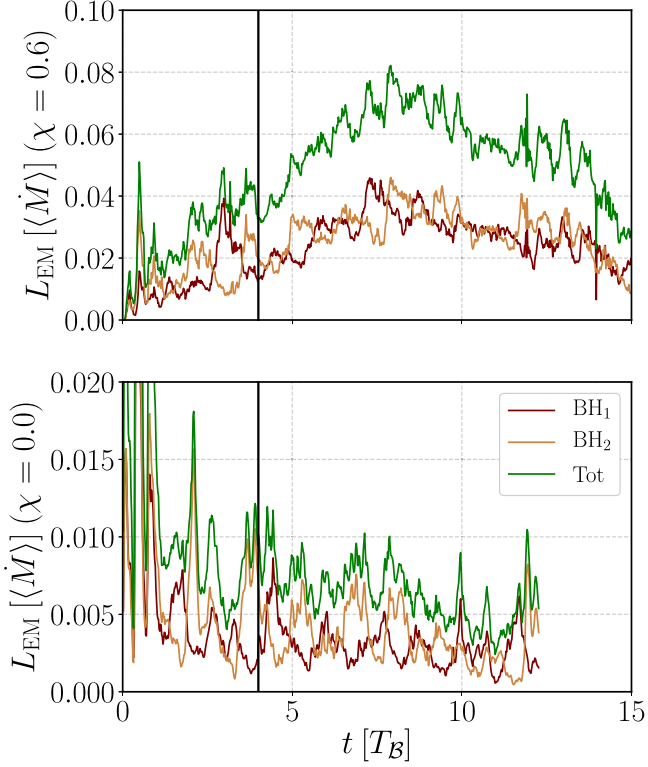


Figure 16. EM luminosity evolution in the BH frame from a sphere at $r = 10M$ for S06 (upper panel) and S0 (lower panel).

3.4. Electromagnetic and Hydrodynamical Fluxes

In this section we analyze the extraction of energy from the system in two forms: outward electromagnetic luminosities, arising from a Poynting flux, and unbound material. In particular, we analyze how these energy fluxes change with spin and how their variability is characterized by the same periodicity as the accretion. The electromagnetic luminosity from each minidisk evaluated in the BH frame is:

$$L_{\text{EM}}(t, \bar{r}) = \oint_{\bar{r}} d\bar{A} \mathcal{S}^{\bar{r}}, \quad (17)$$

where the Poynting flux is $\mathcal{S}^{\bar{r}} := (T_{\text{EM}})^{\bar{r}} \bar{r}$. In Figure 16, we plot the emission measure (EM) luminosity as a function of time for S06 and S0, evaluated on spheres of radius $\bar{r} = 10M$ that follow each black hole. These luminosities are normalized to the average accretion rate $\langle \dot{M} \rangle = 0.002$, so they are equivalent to the rest-mass efficiency of the jets. The most noteworthy element in Figure 16 is that the EM luminosity is an order of magnitude larger in S06 than S0. In both S06 and S0 the EM luminosities are variable, and in both a Fourier power spectrum reveals a periodic modulation at the orbital frequency of the circumbinary disk's inner edge, i.e., the “lump” frequency, see Figure 17. However, in S06 there is an additional modulation of similar amplitude at twice the beat frequency, proving it is tied closely to accretion. In S0, there are no clear long-term trends, whereas in S06, there is a secular growth of L_{EM} until $7.5T_B$, when it starts declining.

The instantaneous efficiency $\eta = L_{\text{EM}}(t)/\dot{M}(t)$ increases during the first several orbits, saturating at ≈ 0.05 in the case of S06, but an order of magnitude lower for S0, as can be seen in Figure 18. The efficiency in S06 with spin parameter 0.6 is

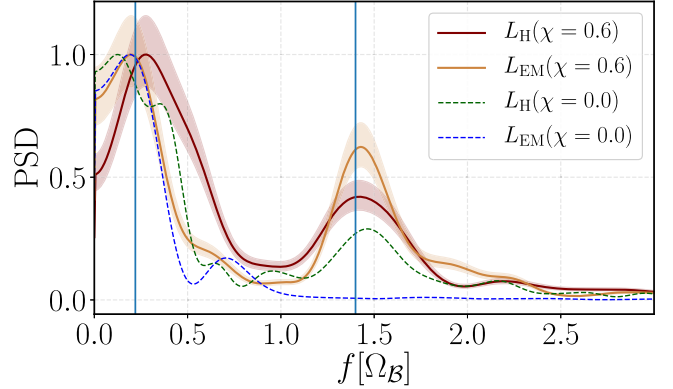


Figure 17. Power spectral density of the hydro (L_H) and EM luminosities (L_{EM}) for S06 (thick lines) and S0 (dashed lines) at $100M$ using a Welch algorithm with a Hamming window size and a frequency of $10M$. The confidence intervals at 3σ are shown as shadowed areas for S06. The two main peaks are given by twice the beat frequency, $2\Omega_{\text{beat}} = 1.4\Omega_{\text{bin}}$, and the lump accretion periodicity $\sim 0.22\Omega_{\text{bin}}$.

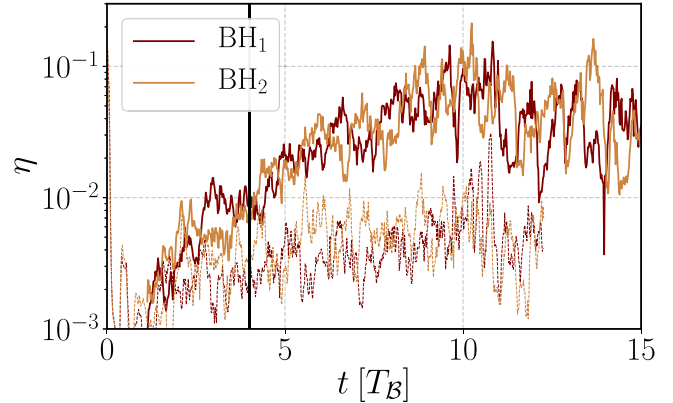


Figure 18. Instantaneous efficiency η of the Poynting flux for S06 (solid lines) and S0 (dashed lines) in the BH frame measured at $\bar{r} = 10M$.

rather larger than 0.013, the value found by De Villiers et al. (2005) for the efficiency of a single BH with specific angular momentum of 0.5 surrounded by a statistically time-steady disk. Both S0 and S06 present a similar secular growth of $\eta(t)$ until $10T_B$, where they slightly drop and plateau. Measuring fluxes in the comoving frame, we found that non-spinning black holes produce negligible EM luminosity, which is consistent with the fundamental idea of the Blandford-Znajek mechanism (Blandford & Znajek 1977; Komissarov 2001) and has been confirmed in many simulations (McKinney & Gammie 2004; De Villiers et al. 2005; Hawley & Krolik 2006; Tchekhovskoy 2015). However, because the BHs are orbiting around the center of mass, this could power additional EM fluxes (Palenzuela et al. 2010b; Neilsen et al. 2011). To capture the electromagnetic fluxes from the entire binary, we move to the center of mass frame and calculate the Poynting flux through a sphere of radius $r = 100M$ surrounding the binary system.

In Figure 19, we plot this quantity for both S06 and S0 as a function of retarded time $t - r/\langle v \rangle$, where $\langle v \rangle$ is the mean velocity of the outflow. We also plot the sum of the Poynting fluxes around each minidisk, measured in the BH comoving frame. We notice that the fluxes in S0 are on average five times larger in the center of mass frame compared with the BH frame, suggesting that there is a kinematic contribution to L_{EM} from the orbital motion of the black holes and possibly from the

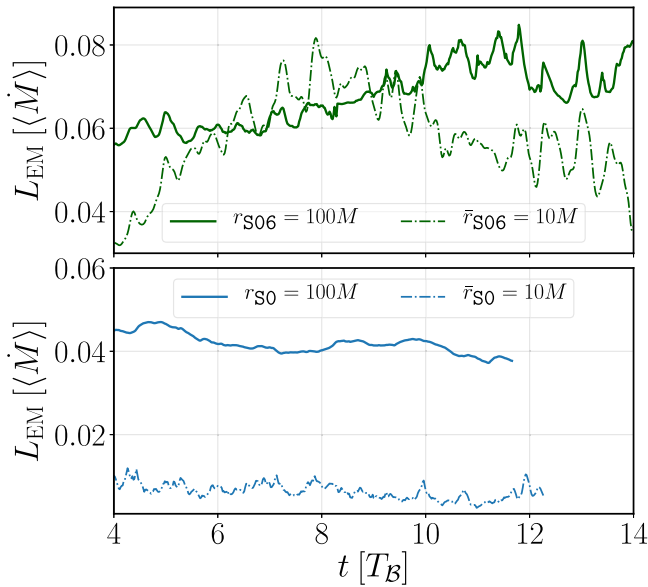


Figure 19. Evolution of the total Poynting flux measured in the BH frame (dashed lines) and in the (inertial) center of mass frame at $100 M$ (solid lines) for both S06 and S0. For the center of mass fluxes, we use the retarded time $t - r/\langle v \rangle$ to account for the delay.

circumbinary disk. The luminosities in S06, on the other hand, differ between frames only by tens of percent, suggesting that the rotation of the black hole dominates the extraction of EM energy here.¹¹ During our simulations, the speed of the black holes remains fairly constant at $v \sim 0.1$ but, closer to the merger, the orbital speed might enhance significantly the electromagnetic luminosity, as seen, e.g., by Palenzuela et al. (2010b), Farris et al. (2012), and Kelly et al. (2021).

To further study the spatial distribution of the electromagnetic flux, in Figure 20, we plot a meridional slice of the Poynting scalar $\mathcal{P} := \mathcal{S}^i \mathcal{S}_i$ for both S06 and S0, averaged in time over half an orbit at $4000M$. The dotted-dashed white lines are defined by $b^2/\rho = 1$, containing the regions that better approximate the magnetically dominated region, while the red solid lines are defined by the region where $hu_t = -1$, where the fluid becomes unbound. As expected, S06 has a much more prominent Poynting jet structure than S0, which has almost zero jet power. The poloidal distribution of \mathcal{P} in S06 around the black hole has a parabolic shape, with most of the flux being emitted at mid-latitudes. Each individual jet shape is similar to those found around single BHs (Nakamura et al. 2018). In both cases, we can also notice the strong (bound) Poynting fluxes generated by magnetic stresses in the disk at the equatorial plane.

In Figure 21, we plot \mathcal{P} , averaged over half an orbit in the corotating frame of the binary, for a sphere of radius $r = 60M$ at the center of mass. In S06 the Poynting flux has a double cone structure that extends to larger polar angles than does the Poynting flux in S0, likely because of interaction between the two jets. On the other hand, in S0, the Poynting flux is distributed on a uniform ring around the axis of the binary. Unfortunately, our simulation coordinates require a cutout in the grid covering the polar axis running through the center of

mass. This prevents an accurate study of the interaction of the jets. Nonetheless, because this cutout is small compared with the angular size of the jets, we are still able to pick out important features.

Besides the electromagnetic fluxes, there are also hydrodynamical fluxes from the system. We define the hydro luminosity as the integral of the energy flux component of the hydrodynamic stress tensor minus the contribution of the rest-mass energy flux at that radius in order to get the “usable” energy flux (Hawley & Krolik 2006):

$$L_H(t, r) := \left(\oint_r dA (T_H)_t^r \right) - \dot{M}_{\text{jet}}. \quad (18)$$

In Figure 22, we plot the hydro luminosity in the center of mass frame as a function of time for both S0 and S06, at different radii, normalized by the averaged value of the accretion rate, so that these luminosities, too, can be described in the language of rest-mass efficiency. In the integral over flux (Equation (18)), we include only fluid elements that are both unbound according to the Bernoulli criterion ($-hu_t > 1$) and moving outward ($u^r > 0$) (see De Villiers et al. 2005). Like the EM luminosity in S06, but not S0, the hydro luminosities are modulated for both spin cases at the “lump” frequency and at twice the beat frequency. Figure 17 shows the Fourier power spectrum for spinning and non-spinning cases. We observe in Figure 22 a secular growth of the hydro fluxes in S06, while in S0 they remain rather constant, with an average efficiency of $\sim 2\%$. Also like the EM case, the hydro energy flux is considerably greater in S06 than S0, but by a factor ~ 5 . Such a contrast resembles the differences between the hydro efficiencies measured in spinning and non-spinning single BH simulations (Hawley & Krolik 2006).

We caution, however, that the luminosities measured at $100M$ may not be the luminosities received at infinity. Energy can be easily converted from EM to hydro or vice versa. Here we quote the values at $100M$ because they are the largest we can measure within our grid. Nonetheless the comparison between S06 and S0 demonstrates clearly that spinning BBH are much more efficient at creating coherent outflows carrying energy both electromagnetically and hydrodynamically than non-spinning BBH.

4. Discussion

Although a few candidates have been identified, the existence of supermassive black hole binaries has not been confirmed. The direct detection of their gravitational waves by LISA or pulsar timing arrays remains at least a decade into the future. Nevertheless, upcoming wide-field surveys, such as the Vera C. Rubin Observatory, SDSS-V, and DESI, may discover many SMBBH candidates through their electromagnetic emission. To confirm the presence of a SMBBH, we need to build accurate models and predictions of their electromagnetic signatures. Our GRMHD simulations will be useful for this purpose: as a next step, in Gutiérrez et al. (2021), we will use these simulations to extract light curves and spectra using ray-tracing techniques (Noble et al. 2007; d’Ascoli et al. 2018) with different radiation models and different masses. The results in this paper constitute the foundations to interpret the underlying physics of those predictions.

Circumbinary and minidisks accretion onto an equal-mass binary system has been largely studied in the past in the context of 2D α -viscous simulations. These simulations are particularly

¹¹ We have also checked the Poynting luminosity as a function of radius, and we observed that, on average, it has variations of around 30% far from the source, which is expected as we lose resolution and the outflow interacts with the atmosphere floor of the simulation.

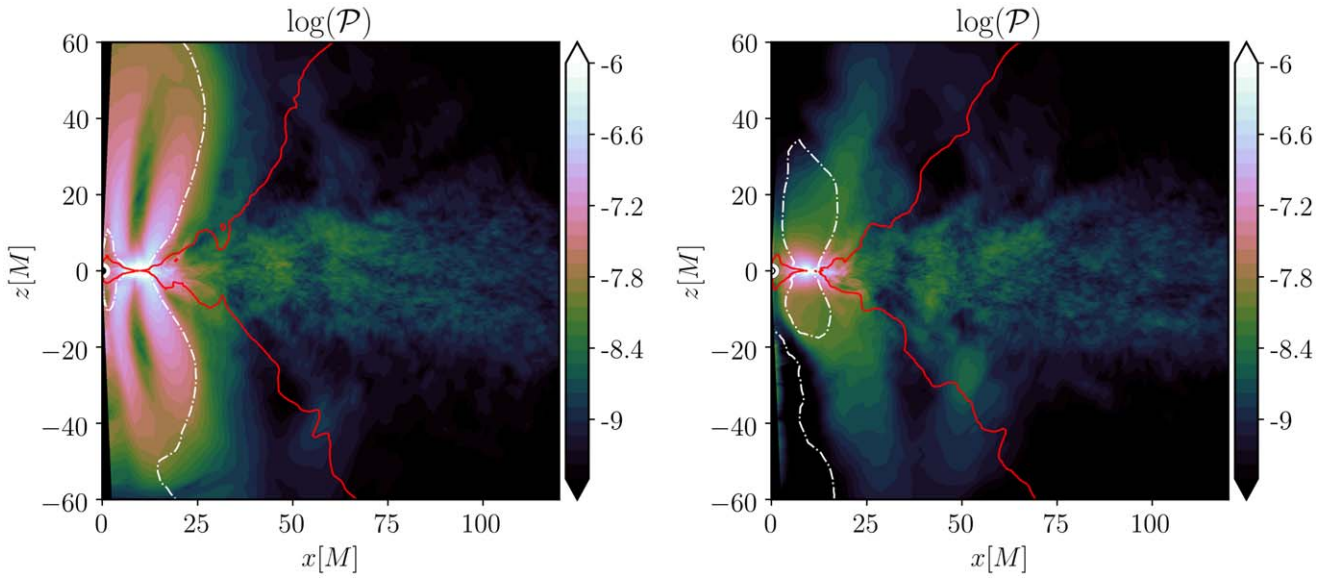


Figure 20. Meridional plot of a time average Poynting scalar for BH₁ in S06 (left) and in S0 (right). The black hole is at $x \sim 10M$ and the center of mass is at $x = 0M$. The red lines represent the division between bound and unbound material, while the dotted-dashed white lines represent the magnetically dominated material.

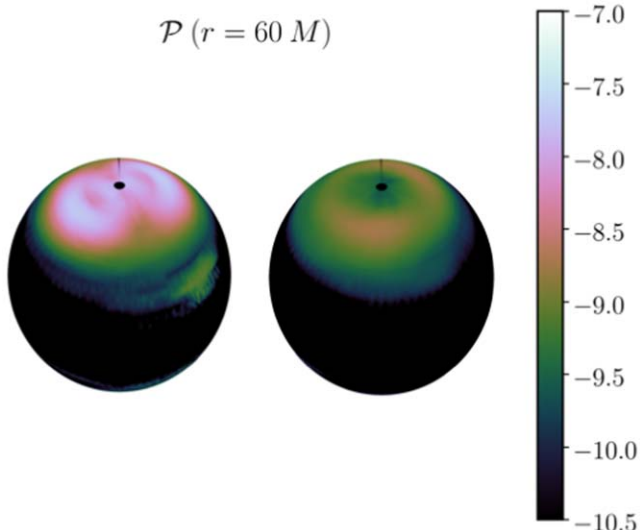


Figure 21. Time average of Poynting scalar \mathcal{P} projected on a sphere of radius $60M$ for spinning (left sphere) and non-spinning (right sphere) for unbound elements of fluid.

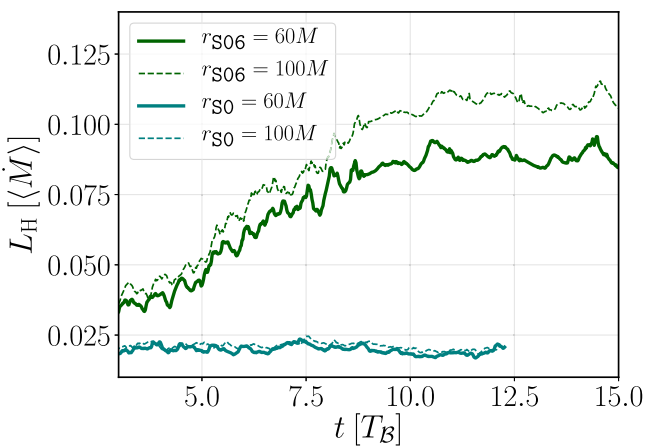


Figure 22. Hydro luminosity as a function of time measured in the center of mass frame for S06 (green lines) and S0 (blue lines) at different radii.

good for analyzing the very long-term behavior of the system, evolving sometimes for 1000 orbits. Close to the black holes and at close separations, however, the inclusion of 3D MHD and accurate spacetime dynamics becomes necessary in order to describe the proper mechanisms of accretion and outflow. Two-dimensional α -disk simulations are not able to include spin effects, and most of them do not include GR effects (see, however, Ryan & MacFadyen 2017). On the other hand, in this work we analyze the balance of hydro accretion from the circumbinary streams and conventional accretion from the internal stresses of the minidisk; to properly model the latter, we need MHD. Moreover, the presence of a proper black hole, and its horizon, makes the accretion processes entirely self-consistent without adding ad hoc sink conditions as used in Newtonian simulations (see, however, Dittmann & Ryan 2021). Finally, 3D MHD simulations are necessary to model magnetically dominated regions and jets. The connection of the accretion and the production of electromagnetic luminosity was one of the main motivations of this work, and impossible to analyze in 2D hydro simulations.

Recently, Paschalidis et al. (2021) presented GRMHD simulations of a system similar to the one analyzed in this paper: equal-mass, spinning binary black holes approaching merger. It is then interesting to compare our results and highlight the differences with their model and analysis. In their paper, they use a slightly higher spin value ($\chi = 0.75$) and explore different spin configurations, including antialigned and up-down directions with respect to the orbital angular momentum. Their system has different thermodynamics than ours, using an ideal-gas state equation with $\Gamma = 4/3$ and no cooling. Their focus is on the mass budget of the minidisk (as in Bowen et al. 2019) and the electromagnetic luminosity when spin is included. They report that spinning black holes have more massive minidisks and the electromagnetic luminosity is higher, with quantitative measures similar to what we find in this paper.

In our work, we analyze in great detail, for the first time, the accretion mechanisms onto the minidisk and their connection to the circumbinary disk. We show that the BHs accretes in two

different ways: through direct plunging of the stream from the lump's inner edge (that dominates the accretion), and through “conventional” stresses of the circular component orbiting the minidisks. This is qualitatively different from single BHs disks and a direct consequence of the short inflow time determined by $r_{\text{ISCO}}/r_{\text{trunc}}$; for larger separations and higher spins, we expect minidisks to behave closer to conventional single BH disks. Our simulations also differ significantly in the grid setup and initial data. We start our simulations with an evolved circumbinary disk snapshot, taken from Noble et al. (2012), which is already turbulent and presents a lump. (Starting the simulation from a quasi-stationary torus, the lump appears after ~ 100 orbit, once the inner edge has settled.) This is very important to accurately describe the periodicities of the system given by the beat frequency, which is set by the orbital motion of the lump. These quasi-periodicities might be different if the thermodynamics change, e.g., if there is no cooling, although currently there are no sufficiently long 3D GRMHD simulations of circumbinary disks exploring this subject. Interestingly, we found that the Poynting flux is also modulated by the beat frequency. For BBH approaching merger, this constitutes a possible independent observable if this periodicity is translated to jet emission. As expected, for spinning BHs, we also found more powerful Poynting fluxes, in agreement with Paschalidis et al. (2021).

With our careful analysis of the accretion onto the minidisks, we show that a disk-like structure survives for longer as the binary shrinks when the black holes have spin. Further explorations with higher spins will show how far these structures survive very close to merger.

5. Conclusions

We have performed a GRMHD accretion simulation of an equal-mass binary black hole with aligned spins of $a = 0.6M_{\text{BH}}$ approaching merger. We have compared this simulation with a previous non-spinning simulation of the same system, analyzing the main differences in minidisk accretion and the variabilities induced by the circumbinary disk accretion. Our main findings can be summarized as follows:

1. Minidisks in S06, where BHs have aligned spins $\chi = 0.6$, are more massive than in S0, where BHs have zero spins, by a factor of 2. The mass and accretion rate of minidisks have quasi-periodicities determined by the beat frequency in both simulations (see Section 3.2).
2. The material in the minidisk region can be separated into two components of relatively high and low angular momentum. The low angular momentum component mostly plunges directly from the lump edge, forming a strong single-arm stream. The (super) Keplerian angular momentum component of the fluid is determined by the size of the ISCO and the truncation radius. We have shown that most of the minidisk mass in S0 is sub-Keplerian, while in S06 most of the material follows the Keplerian value closely up to the end of the evolution, when it becomes comparable to the low angular momentum component. For binary parameters as in this simulation, we have also predicted a critical value of $\chi \sim 0.45$ for which most of the mass will have low angular momentum relative to the ISCO.
3. The accretion rates at the horizon in S06 and S0 are very similar through the evolution (see Figure 5), as they are

dominated by the plunging material from the lump stream (see Figure 14).

4. In S06 a jet-like structure is formed self-consistently around each BH (see Figure 3, right panel). Due to the black hole spin, there is a well-defined Poynting flux (see Figure 20, left panel) with an efficiency of $\eta \sim 8\%$ (see Figure 18). On the other hand, in S0 the efficiency is closer to $\eta \sim 4\%$, and its Poynting flux is more homogeneous in space (see Figure 20, right panel).
5. The time evolution of the Poynting flux is modulated by the quasi-periodicity of the accretion, determined by the beat frequency. In the spinning case, the fluxes in the comoving frame grow and start decreasing at $7.5T_B$, while in the non-spinning these remain fairly constant.

We thank Eduardo Gutiérrez, Vassilios Mewes, Carlos Lousto, and Alex Dittman for useful discussions. L.C., F.L.A., and M.C., acknowledge support from AST-2009330, AST-754 1028087, AST-1516150, and PHY-1707946. L.C. also acknowledges support from a CONICET (Argentina) fellowship. S.C.N. was supported by AST-1028087, AST-1515982, and OAC-1515969, and by an appointment to the NASA Postdoctoral Program at the Goddard Space Flight Center administrated by USRA through a contract with NASA. J.H.K. was supported by AST-1028111, PHY-1707826, and AST-2009260. D.B.B. is supported by the U.S. Department of Energy through the Los Alamos National Laboratory. Los Alamos National Laboratory is operated by Triad National Security LLC for the National Nuclear Security Administration of the U.S. Department of Energy (Contract No. 89233218CNA000001).

Computational resources were provided by the TACC's Frontera supercomputer allocation No. PHY-20010 and AST-20021. Additional resources were provided by the RIT's BlueSky and Green Prairie Clusters acquired with NSF grants AST-1028087, PHY-0722703, PHY-1229173, and PHY-1726215.

The views and opinions expressed in this paper are those of the authors and not the views of the agencies or the U.S. government.

ORCID iDs

Federico G. Lopez Armengol  <https://orcid.org/0000-0002-4882-5672>
 Manuela Campanelli  <https://orcid.org/0000-0002-8659-6591>
 Scott C. Noble  <https://orcid.org/0000-0003-3547-8306>
 Mark Avara  <https://orcid.org/0000-0001-9562-9677>
 Julian H. Krolik  <https://orcid.org/0000-0002-2995-7717>
 Dennis Bowen  <https://orcid.org/0000-0002-7447-1142>

References

Alam, M. F., Arzoumanian, Z., Baker, P. T., et al. 2021, *ApJS*, 252, 5
 Amaro-Seoane, P., Audley, H., Babak, S., et al. 2017, arXiv:1702.00786
 Artymowicz, P., & Lubow, S. H. 1994, *ApJ*, 421, 651
 Babak, S., Petiteau, A., Sesana, A., et al. 2016, *MNRAS*, 455, 1665
 Baker, J. G., Centrella, J., Choi, D.-I., Koppitz, M., & van Meter, J. 2006, *PhRvL*, 96, 111102
 Barnes, J. E., & Hernquist, L. 1992, *ARA&A*, 30, 705
 Barnes, J. E., & Hernquist, L. 1996, *ApJ*, 471, 115
 Begelman, M. C., Blandford, R. D., & Rees, M. J. 1980, *Natur*, 287, 307
 Blandford, R. D., & Znajek, R. L. 1977, *MNRAS*, 179, 433
 Bogdanović, T., Eracleous, M., & Sigurdsson, S. 2009, *ApJ*, 697, 288

Bowen, D. B., Campanelli, M., Krolik, J. H., Mewes, V., & Noble, S. C. 2017, *ApJ*, **838**, 42

Bowen, D. B., Mewes, V., Campanelli, M., et al. 2018, *ApJL*, **853**, L17

Bowen, D. B., Mewes, V., Noble, S. C., et al. 2019, *ApJ*, **879**, 76

Campanelli, M., Lousto, C. O., Marronetti, P., & Zlochower, Y. 2006a, *PhRvL*, **96**, 111101

Campanelli, M., Lousto, C. O., & Zlochower, Y. 2006b, *PhRvD*, **74**, 041501

Campanelli, M., Lousto, C. O., & Zlochower, Y. 2006c, *PhRvD*, **74**, 084023

Campanelli, M., Lousto, C. O., Zlochower, Y., Krishnan, B., & Merritt, D. 2007, *PhRvD*, **75**, 064030

Cattorini, F., Giacomazzo, B., Haardt, F., & Colpi, M. 2021, *PhRvD*, **103**, 103022

Chapon, D., Mayer, L., & Teyssier, R. 2013, *MNRAS*, **429**, 3114

Combi, L., Armengol, F. G. L., Campanelli, M., et al. 2021, *PhRvD*, **104**, 044041

d'Ascoli, S., Noble, S. C., Bowen, D. B., et al. 2018, *ApJ*, **865**, 140

De Villiers, J.-P., & Hawley, J. F. 2003, *ApJ*, **592**, 1060

De Villiers, J.-P., Hawley, J. F., Krolik, J. H., & Hirose, S. 2005, *ApJ*, **620**, 878

Derdzinski, A., D'Orazio, D., Duffell, P., Haiman, Z., & MacFadyen, A. 2021, *MNRAS*, **501**, 3540

Derdzinski, A. M., D'Orazio, D., Duffell, P., Haiman, Z., & MacFadyen, A. 2019, *MNRAS*, **486**, 2754

Dittmann, A., & Ryan, G. 2021, *ApJ*, **921**, 71

D'Orazio, D. J., Haiman, Z., Duffell, P., MacFadyen, A., & Farris, B. 2016, *MNRAS*, **459**, 2379

D'Orazio, D. J., Haiman, Z., & MacFadyen, A. 2013, *MNRAS*, **436**, 2997

D'Orazio, D. J., Haiman, Z., & Schiminovich, D. 2015, *Natur*, **525**, 351

Dotti, M., Colpi, M., Haardt, F., & Mayer, L. 2007, *MNRAS*, **379**, 956

Dotti, M., Montuori, C., Decarli, R., et al. 2009a, *MNRAS*, **398**, L73

Dotti, M., Ruszkowski, M., Paredi, L., et al. 2009b, *MNRAS*, **396**, 1640

Dotti, M., Sesana, A., & Decarli, R. 2012, *AdAst*, **2012**, 940568

Duffell, P. C., D'Orazio, D., Derdzinski, A., et al. 2020, *ApJ*, **901**, 25

East, W. E., Ramazanoğlu, F. M., & Pretorius, F. 2012, *PhRvD*, **86**, 104053

Escala, A., Larson, R. B., Coppi, P. S., & Mardones, D. 2004, *ApJ*, **607**, 765

Escala, A., Larson, R. B., Coppi, P. S., & Mardones, D. 2005, *ApJ*, **630**, 152

Farris, B. D., Duffell, P., MacFadyen, A. I., & Haiman, Z. 2014a, *ApJ*, **783**, 134

Farris, B. D., Duffell, P., MacFadyen, A. I., & Haiman, Z. 2014b, *MNRAS*, **446**, L36

Farris, B. D., Duffell, P., MacFadyen, A. I., & Haiman, Z. 2015a, *MNRAS*, **446**, L36

Farris, B. D., Duffell, P., MacFadyen, A. I., & Haiman, Z. 2015b, *MNRAS*, **447**, L80

Farris, B. D., Gold, R., Paschalidis, V., Etienne, Z. B., & Shapiro, S. L. 2012, *PhRvL*, **109**, 221102

Farris, B. D., Liu, Y. T., & Shapiro, S. L. 2011, *PhRvD*, **84**, 024024

Giacomazzo, B., Baker, J. G., Miller, M. C., Reynolds, C. S., & van Meter, J. R. 2012, *ApJL*, **752**, L15

Graham, M. J., Djorgovski, S. G., Stern, D., et al. 2015a, *Natur*, **518**, 74

Graham, M. J., Djorgovski, S. G., Stern, D., et al. 2015b, *MNRAS*, **453**, 1562

Gutiérrez, E. M., Combi, L., Noble, S. C., et al. 2021, arXiv:2112.09773

Hawley, J. F., & Krolik, J. H. 2006, *ApJ*, **641**, 103

Healy, J., & Lousto, C. O. 2018, *PhRvD*, **97**, 084002

Hemberger, D. A., Lovelace, G., Loredo, T. J., et al. 2013, *PhRvD*, **88**, 064014

Hirose, S., Krolik, J. H., De Villiers, J.-P., & Hawley, J. F. 2004, *ApJ*, **606**, 1083

Kelly, B. J., Baker, J. G., Etienne, Z. B., Giacomazzo, B., & Schnittman, J. 2017, *PhRvD*, **96**, 123003

Kelly, B. J., Eteinne, Z. B., Golomb, J., et al. 2021, *PhRvD*, **103**, 063039

Kelly, B. J., Etienne, Z. B., Golomb, J., et al. 2021, *PhRvD*, **103**, 063039

Kesden, M., Gerosa, D., Berti, E., O'Shaughnessy, R., & Sperhake, U. 2014, *APS Meeting*, C15.004

Khan, F. M., Mirza, M. A., & Holley-Bockelmann, K. 2019, *MNRAS*, **492**, 256

Komissarov, S. S. 2001, *MNRAS*, **326**, L41

Krolik, J. H., Hawley, J. F., & Hirose, S. 2005, *ApJ*, **622**, 1008

Krolik, J. H., Volonteri, M., Dubois, Y., & Devriendt, J. 2019, *ApJ*, **879**, 110

Lin, D. N. C., & Papaloizou, J. 1979, *MNRAS*, **188**, 191

Liu, F. K., Wu, X.-B., & Cao, S. L. 2003, *MNRAS*, **340**, 411

Liu, T., Gezari, S., Ayers, M., et al. 2019, *ApJ*, **884**, 36

Lopez Armengol, F. G., Combi, L., Campanelli, M., et al. 2021, *ApJ*, **913**, 16

Lousto, C. O., & Healy, J. 2015, *PhRvL*, **114**, 141101

Lousto, C. O., & Healy, J. 2019, *PhRvD*, **99**, 064023

Lousto, C. O., Healy, J., & Nakano, H. 2016, *PhRvD*, **93**, 044031

Ma, S., Giesler, M., Scheel, M. A., & Varma, V. 2021, *PhRvD*, **103**, 084029

MacFadyen, A. I., & Milosavljević, M. 2008, *ApJ*, **672**, 83

Mayer, L. 2013, *CQGra*, **30**, 244008

Mayer, L., Kazantzidis, S., Madau, P., et al. 2007, *Sci*, **316**, 1874

McKinney, J. C., & Gammie, C. F. 2004, *ApJ*, **611**, 977

Merritt, D. 2004, in *Coevolution of Black Holes and Galaxies*, ed. L. C. Ho (Cambridge: Cambridge Univ. Press), 263

Merritt, D. 2006, *RPPh*, **69**, 2513

Merritt, D., & Ekers, R. D. 2002, *Sci*, **297**, 1310

Merritt, D., & Milosavljević, M. 2005, *LRR*, **8**, 8

Mihos, J. C., & Hernquist, L. 1996, *ApJ*, **464**, 641

Miranda, R., Muñoz, D. J., & Lai, D. 2017, *MNRAS*, **466**, 1170

Mirza, M. A., Tahir, A., Khan, F. M., et al. 2017, *MNRAS*, **470**, 940

Moesta, P., Alic, D., Rezzolla, L., Zanotti, O., & Palenzuela, C. 2012, *ApJL*, **749**, L32

Moody, M. S. L., Shi, J.-M., & Stone, J. M. 2019, *ApJ*, **875**, 66

Mösta, P., Taam, R. E., & Duffell, P. C. 2019, *ApJL*, **875**, L21

Mundim, B. C., Nakano, H., Yunes, N., et al. 2014, *PhRvD*, **89**, 084008

Muñoz, D. J., & Lai, D. 2016, *ApJ*, **827**, 43

Muñoz, D. J., Lai, D., Kratter, K., & Miranda, R. 2020, *ApJ*, **889**, 114

Muñoz, D. J., & Lithwick, Y. 2020, *ApJ*, **905**, 106

Muñoz, D. J., Miranda, R., & Lai, D. 2019, *ApJ*, **871**, 84

Nakamura, M., Asada, K., Hada, K., et al. 2018, *ApJ*, **868**, 146

Neilsen, D., Lehner, L., Palenzuela, C., et al. 2011, *PNAS*, **108**, 12641

Noble, S. C., Gammie, C. F., McKinney, J. C., & Del Zanna, L. 2006, *ApJ*, **641**, 626

Noble, S. C., Krolik, J. H., Campanelli, M., et al. 2021, *ApJ*, **922**, 175

Noble, S. C., Krolik, J. H., & Hawley, J. F. 2009, *ApJ*, **692**, 411

Noble, S. C., Leung, P. K., Gammie, C. F., & Book, L. G. 2007, *CQGra*, **24**, 259

Noble, S. C., Mundim, B. C., Nakano, H., et al. 2012, *ApJ*, **755**, 51

Paczynski, B. 1977, *ApJ*, **216**, 822

Palenzuela, C., Garrett, T., Lehner, L., & Liebling, S. L. 2010a, *PhRvD*, **82**, 044045

Palenzuela, C., Lehner, L., & Liebling, S. L. 2010b, *Sci*, **329**, 927

Papaloizou, J., & Pringle, J. E. 1977, *MNRAS*, **181**, 441

Park, S., Linsen, L., Kreylos, O., Owens, J., & Hamann, B. 2006, *IEEE Trans. Vis. Comput. Graph.*, **12**, 243

Paschalidis, V., Bright, J., Ruiz, M., & Gold, R. 2021, *ApJL*, **910**, L26

Pretorius, F. 2005, *PhRvL*, **95**, 121101

Reardon, D. J., Hobbs, G., Coles, W., et al. 2016, *MNRAS*, **455**, 1751

Rodriguez, C., Taylor, G. B., Zavala, R. T., et al. 2006, *ApJ*, **646**, 49

Roedig, C., Krolik, J. H., & Miller, M. C. 2014, *ApJ*, **785**, 115

Ryan, G., & MacFadyen, A. 2017, *ApJ*, **835**, 199

Saade, M. L., Stern, D., Brightman, M., et al. 2020, *ApJ*, **900**, 148

Schoenmakers, A. P., de Bruyn, A. G., Rottgering, H. J. A., van der Laan, H., & Kaiser, C. R. 2000, *MNRAS*, **315**, 371

Sesana, A., & Khan, F. M. 2015, *MNRAS*, **454**, L66

Sesana, A., Roedig, C., Reynolds, M. T., & Dotti, M. 2012, *MNRAS*, **420**, 860

Shi, J.-M., & Krolik, J. H. 2015, *ApJ*, **807**, 131

Shi, J.-M., Krolik, J. H., Lubow, S. H., & Hawley, J. F. 2012, *ApJ*, **749**, 118

Springel, V., Matteo, T. D., & Hernquist, L. 2005, *ApJL*, **620**, L79

Tchekhovskoy, A. 2015, in *The Formation and Disruption of Black Hole Jets*, ed. I. Contopoulos, D. Gabuzda, & N. Kylafis, Vol. 414 (Berlin: Springer), 45

Tiede, C., Zrake, J., MacFadyen, A., & Haiman, Z. 2020, *ApJ*, **900**, 43

Tóth, G. 2000, *JCoPh*, **161**, 605

Valtonen, M. J., Nilsson, K., Sillanpää, A., et al. 2006, *ApJL*, **643**, L9

Varma, V., Scheel, M. A., & Pfeiffer, H. P. 2018, *PhRvD*, **98**, 104011

Zilhão, M., & Noble, S. C. 2014, *CQGra*, **31**, 065013

Zilhão, M., Noble, S. C., Campanelli, M., & Zlochower, Y. 2015, *PhRvD*, **91**, 024034

Zlochower, Y., Nakano, H., Mundim, B. C., et al. 2016, *PhRvD*, **93**, 124072

Zrake, J., Tiede, C., MacFadyen, A., & Haiman, Z. 2021, *ApJL*, **909**, L13

Zurek, W. H., & Benz, W. 1986, *ApJ*, **308**, 123